On the Formation and Maintenance of the Interannual Variability of the North Atlantic Oscillation

YANG YANG[a,b] X. SAN LIANG[c,d,e,f] AND WEI-BANG HE[g]

[a] State Key Laboratory of Marine Environmental Science, College of Ocean and Earth Sciences, Xiamen University, Xiamen, China
[b] Department of Physical Oceanography, College of Ocean and Earth Sciences, Xiamen University, Xiamen, China
[c] Artificial Intelligence Department, Division of Frontier Research, Southern Marine Laboratory, Zhuhai, China
[d] CMA–FDU Joint Laboratory of Marine Meteorology, Department of Atmospheric and Oceanic Sciences, Fudan University, Shanghai, China
[e] Institute of Atmospheric Sciences, Fudan University, Shanghai, China
[f] IRDR ICoE on Risk Interconnectivity and Governance on Weather/Climate Extremes Impact and Public Health, Fudan University, Shanghai, China
[g] Department of Atmospheric Sciences, School of Ocean and Earth Science and Technology, University of Hawai'i at Mānoa, Honolulu, Hawaii

(Manuscript received 2 June 2023, in final form 13 November 2023, accepted 16 November 2023)

ABSTRACT: Motivated by the observation that the interannual variability of the North Atlantic Oscillation (NAO) is associated with the ensemble emergence of individual NAO events occurring on the intraseasonal time scale, one naturally wonders how the intraseasonal processes cause the interannual variability and what the dynamics are underlying the multiscale interaction. Using a novel time-dependent and spatially localized multiscale energetics formalism, this study investigates the dynamical sources for the NAO events with different phases and interannual regimes. For the positive-phase events (NAO^+), the intraseasonal-scale kinetic energy (K^1) over the North Atlantic sector is significantly enhanced for NAO^+ occurring in the negative NAO winter regime (NW), compared to those in the positive winter regime (PW). It is caused by the enhanced inverse cascading from synoptic transients and reduced energy dispersion during the life cycle of NAO^+ in NW. For the negative-phase events (NAO^-), K^1 is significantly larger during the early and decay stages of NAO^- in NW than that in PW, whereas the reverse occurs in the peak stage. Inverse cascading and baroclinic energy conversion are primary drivers in the formation of the excessive K^1 during the early stage of NAO^- in NW, whereas only the latter contributes to the larger K^1 during the decay stage of NAO^- in NW compared to that in PW. The barotropic transfer from the mean flow, inverse cascading, and baroclinic energy conversion are all responsible for the strengthened K^1 in the peak stage of NAO^- in PW.

KEYWORDS: North Atlantic Oscillation; Energy budget/balance; Interannual variability; Intraseasonal variability

1. Introduction

The North Atlantic Oscillation (NAO) is the most dominant and recursive teleconnection pattern over the extratropical North Atlantic. It is characterized as a planetary-scale dipole oriented meridionally in sea level pressure (SLP) and has an equivalent barotropic vertical structure (Wallace and Gutzler 1981). The dynamical origin of the NAO has been a subject of numerous studies and debates in the past few decades, as it exerts broad influences on the regional and hemispheric weather and climate (e.g., Hurrell et al. 2003).

As a typical low-frequency mode in the atmosphere, the NAO exhibits a broadband of temporal variabilities, ranging from weekly to decadal time scales (Hurrell 1995; Feldstein 2000). Seminal works by Feldstein (2000, 2003) showed that the life cycle of typical NAO events has an *e*-folding time scale of about 10 days, analogous to a stochastic Markov process. Many studies since then sought to describe and understand the growth and decay of NAO patterns on the intraseasonal time scale using daily, rather than monthly or seasonally, averaged data, as a normal practice earlier on (Vallis et al. 2004; Benedict et al. 2004; Jia et al. 2007; Rivière and Orlanski 2007; Barnes and Hartmann 2010; Luo et al. 2015; Song 2016). Contrary points of view have been proposed for the origin of the NAO on the intraseasonal time scale, involving intrinsic and external forcing. Although atmospheric variability on this scale range may be influenced by local air–sea interactions (e.g., Peng et al. 2003; Czaja et al. 2003; Ciasto and Thompson 2004; Nie et al. 2019), or by other forcings such as El Niño–Southern Oscillation (e.g., Brönnimann 2007; Ayarzagüena et al. 2018), the solar radiation (e.g., Kodera 2002; Gray et al. 2013), or the volcanic activity (e.g., Stenchikov et al. 2002; Christiansen 2008), results from both numerical experiments and observations have provided substantial evidence that the NAO is, at least partly, generated and maintained by intrinsic nonlinear interactions in the atmosphere (e.g., Thompson et al. 2003).

One popular intrinsic mechanism states that the low-frequency planetary-scale NAO flow arises from strong interaction with synoptic transients (Lau 1988; Cai and Mak 1990; Nakamura and Wallace 1990; Robinson 2000; Vallis et al. 2004; Jin et al. 2006; Rivière and Orlanski 2007). Eddy forcing and wave breaking processes by synoptic transients have been shown to contribute significantly to the formation of the NAO pattern (Benedict et al. 2004; Woollings et al. 2008; Barnes and Hartmann 2010; Song 2016). Meanwhile, the low-frequency flow also systematically organizes the transient eddies though local instability (Cai and Mak 1990; Lorenz and Hartmann 2003; Jin et al. 2006; Ren et al. 2012), indicating a

Supplemental information related to this paper is available at the Journals Online website: https://doi.org/10.1175/JAS-D-23-0100.s1.

Corresponding author: X. San Liang, x.san.liang@gmail.com

DOI: 10.1175/JAS-D-23-0100.1

two-way interaction between the NAO and synoptic transients. For instance, by performing a momentum budget analysis, Lorenz and Hartmann (2003) proposed a simple positive feedback mechanism that anomalously strong synoptic eddies generated in a band of enhanced westerlies tend to strengthen the convergence of westerly momentum and therefore further accelerate the westerlies, and vice versa. Another intrinsic but less noted mechanism is the interaction between the seasonal mean flow (i.e., the North Atlantic midlatitude jet) and low-frequency perturbations (Simmons et al. 1983; Frederiksen 1983; Sheng and Derome 1991; DeWeaver and Nigam 2000). An early attempt using normal mode analysis of a barotropic model (Simmons et al. 1983) revealed that the horizontally sheared jet stream can generate unstable modes similar to the teleconnection patterns observed in the atmosphere. Subsequently, Frederiksen (1983) examined a three-dimensional (3D) instability model and pointed out that barotropic instability alone is not enough to explain the observed intensity of the low-frequency anomalies, suggesting the importance of baroclinic process in maintaining the NAO pattern.

In addition to intraseasonal variability, the NAO also exhibits significant interannual and longer-term modulations (Hurrell 1995; Watanabe et al. 1999; Cohen et al. 2005; Luo et al. 2012). For example, it is well known that the 1960–70 (1980–2000) is dominated by a negative (positive) NAO climate regime (Hurrell 1995). The forcing mechanism of NAO on these time scales seems more controversial. Contradicting views exist on the NAO's response to the sea surface temperature (SST) in numerical experiments. While some models forced by observed SSTs are capable of reproducing the observed interannual change of the NAO (e.g., Rodwell et al. 1999; Czaja et al. 2003), some are not (e.g., Josey et al. 2001; Cohen et al. 2005). Bretherton and Battisti (2000) provided a note of caution on the physical interpretation of model experiments with prescribed observed SST field, which already contains the atmospheric interannual variability due to the dominant causal forcing from the atmosphere to the ocean on these time scales.

On the other hand, some studies suggested that the long-term variability of the NAO should be interpreted as an ensemble emergence of individual NAO events occurring on the intraseasonal time scale, rather than a climate shifting process in response to external forcings (Feldstein 2000; Cassou et al. 2004; Johnson et al. 2008; Franzke 2009; Luo et al. 2012). Johnson et al. (2008) elaborated upon this perspective by using the self-organizing maps (SOMs), an unsupervised-learning clustering technique. Their result reveals that the interdecadal regime shift of the NAO is related to the change in the occurrence frequency of the positive- or negative-phase NAO events in a certain decadal period, though both phases exist for both regimes. Luo et al. (2012) studied the increasing (decreasing) trend during 1978–90 (1991–2008) in the wintertime mean NAO index and suggested that the occurrence frequency of intraseasonal NAO transitional events (i.e., negative-to-positive or positive-to-negative events) may attribute to the observed decadal trends. While results of these studies highlight the importance of intraseasonal NAO events on the long-term variability of the NAO, they did not examine the causal relations among the covarying background jet stream, the NAO flow and the storm-track eddies on the long time scales. An understanding of this, especially from the time-dependent perspective of multiscale interactions, may help improve the predictability of the NAO on time scales from weeks to years.

In this study, we will address this issue from a novel three-scale (i.e., seasonal mean flow, low-frequency fluctuation, and synoptic transients) energetics point of view, with the aid of an orthogonal scale-decomposition tool, multiscale window transform (MWT), and the MWT-based canonical transfer theory in light of energy conservation across scales (Liang 2016). In section 2, we first introduce the multiscale analysis framework and data used for this study, and then delineates the identification of positive- and negative-phase NAO events. Each group is further divided into two subgroups according to the phase of their interannual regimes. In section 3, we present the statistical and temporal characteristics of these NAO subgroups. The dynamical processes responsible for the distinct features of these events are investigated in section 4. This study is summarized and discussed in section 5.

2. Method and data

a. A localized three-scale energetics framework

Considering that the NAO is essentially an intraseasonal phenomenon with a typical life cycle on the order of 10 days (Feldstein 2003), and that strong interactions exist between the synoptic-scale disturbances (periods less than a week), the low-frequency NAO flow, and the seasonally varying mean flow, we employ a three-scale energetics formalism (Liang 2016) to investigate the nonlinear multiscale interactions among these distinct components. The formalism invokes the use of a scale-decomposition technique, namely, the MWT, and the theory of canonical transfer, as described below.

One of the major issues with traditional energetics formalisms using Reynolds decomposition (e.g., Lorenz 1955) or Fourier transform (e.g., Saltsman 1957) is that localization is lost in the physical dimension where the decomposition is performed. In this study, we only consider decomposition on time scale, and hence localization is lost in time. To retain the local signals, it is common in atmospheric literature to use filters to decompose a field into several components (e.g., $u = \overline{u} + u'$, where $\overline{u}$ and u' stand for the slow manifold and transients of u) and then take the square of each component as the energy of the corresponding filtered field (e.g., $\overline{u}^2$ and u'^2). Unfortunately, treating u'^2 as the localized (i.e., time-dependent) eddy energy is problematic because $u^2 \neq \overline{u}^2 + u'^2$. (Some people argue that there is involved an "interaction energy" $2\overline{u}u'$, but that is confounded with, and hence cannot correctly give, the interscale energy transfer, which is the key in multiscale energetics studies.) To ensure the conservation of the total energy, the decomposition must be orthogonal (i.e., $\overline{\overline{u} \cdot u'} = 0$) so that $\overline{u^2} = \overline{u}^2 + \overline{u'^2}$. It is important to realize that the slow-manifold operator in $\overline{u'^2}$ cannot simply be removed. In fact, multiscale energy is a concept in phase space, such as that in the Fourier power spectrum. It is related to physical energy by the

Parseval relation. A simple illustrative example is provided in the appendix of a previous paper by the author (Yang and Liang 2019). To overcome this difficulty, Liang and Anderson (2007) developed the MWT, a functional analysis tool that allows for an orthogonal decomposition of signals onto several scale windows while retaining their localized information. A distinct feature of the MWT as compared to traditional filtering techniques is that the MWT yields not only the reconstruction, but also the transform coefficients, on a specified scale window. The reconstruction, defined in physical space, is just like the traditional filtered field. But the transform coefficient is a new thing which, as we will see soon, allows for a physically consistent representation of multiscale energy. For example, in this study we need three components, involving the seasonal mean flow (periods $>$ 64 days), the intraseasonal-scale flow (in the 8–64-day period) and the synoptic transients (periods $<$ 8 days). The cutoff period chosen to separate the synoptic and intraseasonal fluctuations is similar to that chosen in previous studies (e.g., Hoskins et al. 1983; Lorenz and Hartmann 2003). A state variable, say, $u(t)$, then can be decomposed into three parts,

$$u(t) = u^{\sim 0}(t) + u^{\sim 1}(t) + u^{\sim 2}(t), \tag{1}$$

where $u^{\sim 0}$, $u^{\sim 1}$, and $u^{\sim 2}$ stand for reconstructions (filtered fields) on the mean, intraseasonal, and synoptic-scale windows. Different from traditional filters, for each reconstruction $u^{\sim \varpi}(t)$ ($\varpi = 0, 1, 2$), there exists a corresponding transform coefficient, $\hat{u}_n^{\sim \varpi}$ (n denotes the discrete time step and the hat is the transform operator) in the MWT framework. The very transform coefficient, defined in phase space, allows for a faithful representation of energy on window ϖ. By the property of marginalization (a property analogous to the Parseval relation), Liang and Anderson (2007) proved that the energy of u on scale window ϖ at time step n is $(\hat{u}_n^{\sim \varpi})^2$ (up to some factor), just as the energy in a power spectrum which is the square of the transform coefficient. Note that $(\hat{u}_n^{\sim \varpi})^2$ is by no means equal to $[u^{\sim \varpi}(t)]^2$.

In this study, we choose the period range of the intraseasonal-scale window as 8–64 days because the lifespan of typical NAO events lies in this band, similar to that implemented in a recent energetics study by Martineau et al. (2020). It should be noted that the *e*-folding time scale (a concept frequently used in NAO literature, i.e., about 10 days for typical NAO events) of a physical process is usually much shorter than the period of that process. For example, Simmons et al. (1983) reported that the teleconnection pattern in their barotropic model has an *e*-folding time scale of about 1 week and a period of about 50 days. Here the cutoff periods (i.e., 8 and 64 days) are chosen because the MWT requires them to be a power of 2 multiplied by the time step size of the data (i.e., 1 day in this study). We have also used 8–32 days as the period range and find that the basic results in this study are unaltered.

Applying the MWT to the primitive equations of the atmosphere, the equations governing the evolution of kinetic energy (KE) on scale window ϖ, denoted as K^{ϖ}, can be derived. Interested readers are referred to Liang (2016) for technical details. The equation is as follows:

$$\begin{aligned}\frac{\partial K^{\varpi}}{\partial t} = & \underbrace{-\nabla\cdot\left[\frac{1}{2}\widehat{(\mathbf{v}\mathbf{v}_h)}^{\sim\varpi}\cdot\hat{\mathbf{v}}_h^{\sim\varpi}\right]}_{D_K^{\varpi}} \\ & \underbrace{+\frac{1}{2}\left[\widehat{(\mathbf{v}\mathbf{v}_h)}^{\sim\varpi}:\nabla\hat{\mathbf{v}}_h^{\sim\varpi}-\nabla\cdot\widehat{(\mathbf{v}\mathbf{v}_h)}^{\sim\varpi}\cdot\hat{\mathbf{v}}_h^{\sim\varpi}\right]}_{\Gamma_K^{\varpi}} \\ & \underbrace{-\nabla\cdot(\hat{\mathbf{v}}^{\sim\varpi}\hat{\Phi}^{\sim\varpi})}_{\Pi^{\varpi}}+\underbrace{(-\hat{\omega}^{\sim\varpi}\hat{\alpha}^{\sim\varpi})}_{B^{\varpi}}+R_K^{\varpi},\end{aligned} \tag{2}$$

where $\mathbf{v} = (\mathbf{v}_h, \omega) = (u, v, \omega)$ is the 3D velocity vector, ∇ is the 3D gradient operator, Φ is the geopotential function, and α is the specific volume. Note that the subscript n is omitted for notational brevity. The colon operator (:) stands for colon product of two dyads such that, for vectors $\mathbf{A}$, $\mathbf{B}$, $\mathbf{C}$, and $\mathbf{D}$, $(\mathbf{AB}):(\mathbf{CD}) = (\mathbf{A}\cdot\mathbf{C})(\mathbf{B}\cdot\mathbf{D})$. The physical meaning of each term on the right-hand side of Eq. (2) is described as follows. The first term on the right-hand side D_K^{ϖ} is the spatial advection of K^{ϖ} by the total flow. The third term Π^{ϖ} is the rate of work done by the geopotential fluxes. Since the geostrophic flow is nondivergent, only the ageostrophic flow contributes to this term (Orlanski and Katzfey 1991). The advection and geopotential flux divergence term represent energy dispersion processes that redistribute energy in the physical space, and therefore will be treated as a combined nonlocal term $D_K^{\varpi} + \Pi^{\varpi}$ in this study. B^{ϖ} is the vertical buoyancy flux on window ϖ (also referred to as the buoyancy/baroclinic energy conversion) that converts available potential energy (APE) to K^{ϖ}. The fourth term Γ_K^{ϖ} is the barotropic KE transfer due to nonlinear interaction. The last term R_K^{ϖ} includes friction and subgrid-scale dissipation. This term is not explicitly diagnosed but treated as the residue of the equation due to unavailability of certain variables from the reanalysis dataset.

Among the various terms in Eq. (2), Γ_K^{ϖ}, referred to as the canonical transfer of KE or barotropic canonical transfer, is particularly important because it measures the energy transferred to window ϖ due to nonlinear interactions. It was first introduced in Liang and Robinson (2005, 2007), and was later rigorously formulated in Liang (2016). Γ_K^{ϖ} satisfies the following conservation property:

$$\sum_{\varpi}\sum_{n}\Gamma_{K,n}^{\varpi} = 0. \tag{3}$$

That is, the sum of KE transfers over all windows and time steps is zero, implying physically there is no net generation or destruction of energy as a whole. This property, though simply stated, does not in general hold for existing energetics formalisms.

In the following, the Reynolds mean–eddy decomposition framework is considered to allow for a direct comparison between canonical transfer and conventional transfer. The KE equations for the mean and eddy in the conventional sense are

$$\frac{\partial K_M}{\partial t} + \nabla\cdot(\bar{\mathbf{v}}K_M) + \cdots = -(\nabla\cdot\overline{\mathbf{v}'\mathbf{v}'})\cdot\bar{\mathbf{v}} \quad \text{and} \tag{4}$$

$$\frac{\partial K_E}{\partial t} + \nabla\cdot\left(\frac{1}{2}\overline{\mathbf{v}\mathbf{v}'^2}\right) + \cdots = -\overline{\mathbf{v}'\mathbf{v}'}:\nabla\bar{\mathbf{v}}, \tag{5}$$

respectively. The overbar and the prime stand for an ensemble mean (practically replaced by a time mean) and the departure from the mean (referred to as the eddy component), respectively. $K_M = (1/2)\bar{\mathbf{v}}^2$ and $K_E = (1/2)\overline{\mathbf{v}'^2}$ are the mean and eddy KE, respectively. Additional terms including the pressure work, the buoyancy conversion and dissipation are not shown in the above equations since they are irrelevant for illustration. The two terms on the right-hand side of Eqs. (4) and (5) have been interpreted as the KE transfer [also referred to as barotropic transfer (BT)] due to eddy–mean flow interaction. Particularly, it has been a convention in literature to calculate $-\overline{\mathbf{v}'\mathbf{v}'} : \nabla\bar{\mathbf{v}}$ and take it as the indicator of barotropic instability.

It is important to note that the BTs in the above conventional equations do not cancel out. This is not what one would expect, because physically a transfer process should only redistribute energy between the two scale windows, without generating or destroying energy as a whole. This problem, often overlooked, actually has long been known (e.g., Holopainen 1978; Plumb 1983). It has just been systematically addressed by Liang and Robinson (2005, 2007) and Liang (2016) in the development of their MWT-based multiscale energetics formalism.

In these systematic studies, they first showed (Liang and Robinson 2007), and later on rigorously proved (Liang 2016), that the barotropic canonical transfer within the Reynolds decomposition framework should be

$$\Gamma = \frac{1}{2}\{[\nabla\cdot(\overline{\mathbf{v}'\mathbf{v}'})]\cdot\bar{\mathbf{v}} - (\overline{\mathbf{v}'\mathbf{v}'}) : \nabla\bar{\mathbf{v}}\}. \tag{6}$$

Accordingly, the mean and eddy KE equations are

$$\frac{\partial K_M}{\partial t} + \nabla\cdot\left(\bar{\mathbf{v}}K_M + \frac{1}{2}\overline{\mathbf{v}'\mathbf{v}'}\cdot\bar{\mathbf{v}}\right) + \cdots = -\Gamma \quad \text{and} \tag{7}$$

$$\frac{\partial K_E}{\partial t} + \nabla\cdot\left(\frac{1}{2}\overline{\mathbf{v}\mathbf{v}'^2} + \frac{1}{2}\overline{\mathbf{v}'\mathbf{v}'}\cdot\bar{\mathbf{v}}\right) + \cdots = \Gamma, \tag{8}$$

respectively. In contrast to the conventional formalism, the BTs in the above two equations sum to zero, indicating that the canonical transfer conserves energy over the two scale windows. Extensive validation of the canonical transfer has been done. For example, Liang and Robinson (2007) showed that the canonical transfer verifies the localized instability structure of a benchmark barotropic jet stream model, while the conventional transfer formula fails. More appealing properties of a canonical transfer include that it satisfies the Jacobian identity, and bears a Lie bracket form, which reminds one of the Poisson bracket in theoretical physics, Hamiltonian dynamics in particular, indicating that canonical transfer is indeed more physically relevant.

Γ_K^{ϖ} needs to be further divided to single out the interaction between two specified scale windows, which is fulfilled by the "interaction analysis" procedure as explained in detail by Liang and Robinson (2005). Here we present a brief description of this procedure. Note that all individual terms in Γ_K^{ϖ} bear a form of triple product like $\Gamma_K^{\varpi} = \hat{\xi}^{\sim\varpi}\widehat{(\varphi\psi)}^{\sim\varpi}$. Take window $\varpi = 1$ (the focus of this study) for instance, it can be decomposed as follows:

$$\Gamma_K^1 = \hat{\xi}^{\sim 1}\widehat{(\varphi\psi)}^{\sim 1} = \hat{\xi}^{\sim 1}\left(\sum_{\varpi_1=0}^{2}\varphi^{\sim\varpi_1}\sum_{\varpi_2=0}^{2}\psi^{\sim\varpi_2}\right)^{\sim 1} = \underbrace{\hat{\xi}^{\sim 1}\left[\widehat{\left(\varphi^{\sim 0}\psi^{\sim 0}\right)}^{\sim 1} + \widehat{\left(\varphi^{\sim 0}\psi^{\sim 1}\right)}^{\sim 1} + \widehat{\left(\varphi^{\sim 1}\psi^{\sim 0}\right)}^{\sim 1}\right]}_{\Gamma_K^{0\to 1}}$$

$$+ \underbrace{\hat{\xi}^{\sim 1}\left[\widehat{\left(\varphi^{\sim 1}\psi^{\sim 2}\right)}^{\sim 1} + \widehat{\left(\varphi^{\sim 2}\psi^{\sim 1}\right)}^{\sim 1} + \widehat{\left(\varphi^{\sim 2}\psi^{\sim 2}\right)}^{\sim 1}\right]}_{\Gamma_K^{2\to 1}} + \underbrace{\hat{\xi}^{\sim 1}\left[\widehat{\left(\varphi^{\sim 0}\psi^{\sim 2}\right)}^{\sim 1} + \widehat{\left(\varphi^{\sim 2}\psi^{\sim 0}\right)}^{\sim 1}\right]}_{\Gamma_K^{0\oplus 2\to 1}} + \underbrace{\hat{\xi}^{\sim 1}\widehat{\left(\varphi^{\sim 1}\psi^{\sim 1}\right)}^{\sim 1}}_{\Gamma_K^{1\to 1}}, \tag{9}$$

where $\Gamma_K^{0\to 1}$ represents the barotropic energy transfer rate from the mean flow window ($\varpi = 0$) to the intraseasonal window ($\varpi = 1$), $\Gamma_K^{2\to 1}$ represents the transfer rate from the synoptic window ($\varpi = 2$) to the intraseasonal window ($\varpi = 1$), $\Gamma_K^{0\oplus 2\to 1}$ represents the contribution from the mean-synoptic interaction to the intraseasonal window, and $\Gamma_K^{1\to 1}$ is the transfer rate through interaction among the intraseasonal fluctuations themselves.

It is worth noticing that energetics analysis of the atmospheric low-frequency teleconnection patterns is not new. Simmons et al. (1983) found that the most rapidly growing mode in a barotropic jet model has a period close to 50 days. The unstable mode is found to extract KE from the background flow and maximized in the jet exit region. Using a two-layer quasigeostrophic channel model, Cai and Mak (1990) analyzed the spectral energetics of the simulated flow and found that the low-frequency planetary waves are sustained by high-frequency synoptic-scale waves through inverse cascading. By dividing the original flow into a time-mean, a low- (>10-day period), and a high-frequency (<10-day period) component, Sheng and Derome (1991) studied the time-mean feature of the three-scale energetics in the Northern Hemisphere based on a 5-yr reanalysis dataset and found that the barotropic energy transfer from both the mean flow and the high-frequency transients are primary energy sources for the low-frequency variability. Subsequently, many numerical and observational studies provided evidence that the two barotropic processes play important roles in maintaining the low-frequency

teleconnection patterns (Higgins and Schubert 1994; Jiang et al. 2013; Luo et al. 2015; Castanheira and Marques 2019). Conversely, another group of studies emphasized that the baroclinic energy conversion, a well-known process that dominates the generation of high-frequency transients in the atmosphere, is also an important and even a larger source of energy for the low-frequency variability compared to the barotropic processes (e.g., Higgins and Schubert 1994; Martineau et al. 2020).

The above-mentioned works have provided helpful insights into the energetics of the low-frequency variability in the atmosphere. However, most of these studies are conducted from a time-mean perspective so that they did not describe the energetic processes underlying the growth and decay of the NAO life cycle. More importantly, none of the studies to date have examined the interannual variability of the NAO events from a multiscale energetics perspective. As will be shown later, new insights can be gained by considering the interannual regimes of the NAO separately. Moreover, different from previous studies using simple or idealized models, the multiscale energy budget formalism used in this study is derived from the primitive equations of atmosphere and hence full physics are embedded in the diagnostic metrics. Therefore, the MWT-based theory of canonical transfer and time-dependent analysis allow for an investigation of spatiotemporal characteristics of the energetics on a more conceptually and physically rigorous footing.

The energetics analysis is performed on time series extending through the entire year, but only data for the boreal winter months [December–February (DJF)] are analyzed in this study because the NAO is most active during the winter season (e.g., Hurrell et al. 2003).

b. Data

In this study, the daily outputs from the Twentieth Century Reanalysis (20CR) version 2 (Compo et al. 2011) distributed by the National Oceanic and Atmospheric Administration (NOAA) are used. This dataset has a horizontal resolution of $2° \times 2°$ and provides a long-term state estimate of the global atmosphere from 1871 to 2012. The 20CR project uses an ensemble Kalman filter assimilation scheme (Whitaker and Hamill 2002) to assimilate surface pressure observations every 6 h. The 142-yr-long dataset yields a considerably larger data sample compared to other widely used atmospheric reanalysis. Previous model–observation and interreanalysis verifications indicate that the 20CR has a good performance in reproducing the observed long-term features of the NAO (e.g., Compo et al. 2011; Woollings et al. 2015).

c. NAO event identification

Following the conventional definition of the NAO (e.g., Barnes and Hartmann 2010), we define the NAO spatial pattern as the leading empirical orthogonal function (EOF) of the monthly-mean SLP anomaly over the North Atlantic sector (20°–85°N, 90°W–50°E), which accounts for 33.7% of the total variance of the monthly SLP. The seasonal cycle and linear trend are removed from the monthly-mean SLP field prior to the EOF analysis (notice that this procedure does not change the result). The SLP field is also properly area weighted prior to the EOF analysis to account for the uneven grid size (e.g., Barnes and Hartmann 2010). By convention, the positive phase of the NAO pattern corresponds to a positive lobe across the subtropical Atlantic and a negative lobe at high latitudes (Fig. 1a). The paired monthly-mean principal component (PC) time series is averaged in each winter (DJF) and normalized by its standard deviation to obtain the wintertime-mean NAO index, which exhibits significant variabilities on interannual and longer time scales (Fig. 1b). It can be also seen that the predominantly negative regime in 1960–70 and positive regime in 1980–2000, as reported in observation records (Hurrell 1995), are well reproduced in 20CR, demonstrating the high degree of fidelity of this dataset. In this study, positive (negative) NAO winters are determined when the wintertime-mean NAO index exceeds $+0.5$ (-0.5) standard deviation.

To investigate the evolution of the NAO events occurring on the intraseasonal time scale, we also need an index with a daily temporal resolution. This index is obtained by the following procedures, which is similar to the ones used in previous studies (e.g., Jia et al. 2007; Benedict et al. 2004; Kunz et al. 2009; Barnes and Hartmann 2010). First, the seasonal cycle and linear trends are removed from the original daily SLP field (again this procedure does not significantly change the result). Then a low-pass filter is applied to remove the synoptic-scale (periods < 8 days) transients. Finally, the treated SLP field is projected onto the NAO pattern and normalized by its standard deviation to obtain the daily NAO index.

The positive- and negative-phase NAO events, denoted as NAO^+ and NAO^- for short, are identified as follows. Local maximum and minimum are searched in the daily NAO index time series. Once the maximum (minimum) value exceeds $+0.5$ (-0.5) standard deviation, an NAO^+ (NAO^-) event is identified, and the peak day is labeled as the lag 0 day (also referred to as the onset day). The 15 neighboring days before and after the onset day (in all 31 days) are selected out accordingly. The 31-day window is chosen so because it is sufficiently longer than the lifetime of typical NAO events. When two or more peaks are detected within the 31-day window, only the one with the largest amplitude is kept. We further discard events if the growth and decay are nonmonotonic between lag -5 and $+5$ days, to make sure that our analysis does not include any highly oscillatory event whose index drops and rise back as a secondary peak.

To further investigate the interannual regimes of the NAO, we delineate four subgroups from the identified events by checking whether or not an event occurs in the positive or negative NAO winters (indicated by the wintertime-mean NAO index as described above). If an NAO^+ (NAO^-) event occurs in a positive NAO winter, then it is defined as a NAO^+_{PW} (NAO^-_{PW}) event. Similarly, if an NAO^+ (NAO^-) event occurs in a negative NAO winter, then it is defined as a NAO^+_{NW} (NAO^-_{NW}) event.

3. Spatiotemporal characteristics of the NAO events in different interannual regimes

a. Regression pattern

In this section, we present the distinct characteristics of the NAO events in the positive and negative NAO winters.

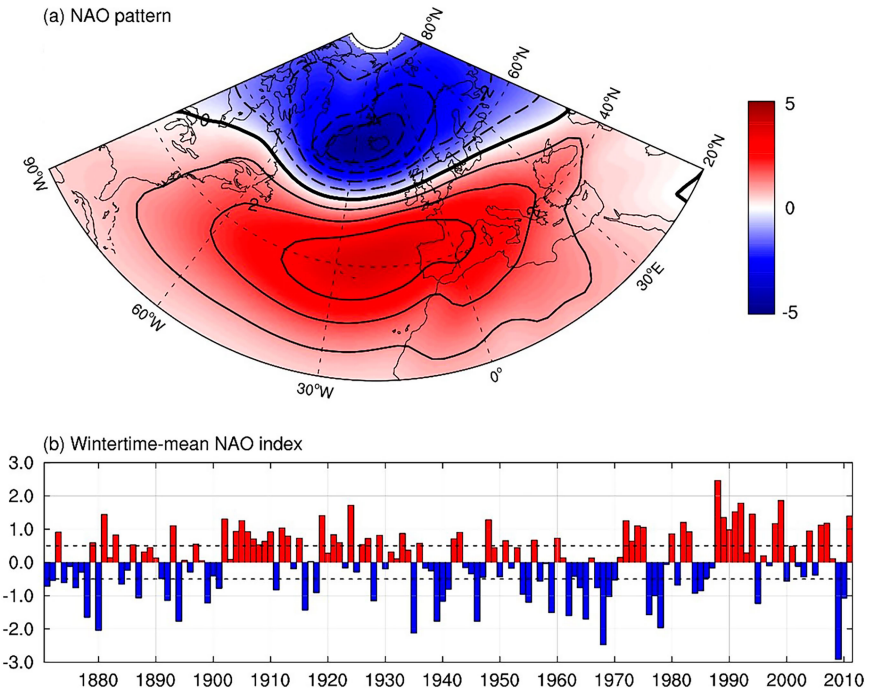

FIG. 1. (a) Leading EOF of the wintertime (DJF) monthly-mean SLP anomalies over the North Atlantic sector (20°–85°N, 90°W–20°E). The spatial pattern, in terms of amplitude (unit: hPa), is obtained by regressing the SLP anomalies onto the standardized PC time series. (b) Standardized wintertime mean PC time series associated with the leading EOF pattern, referred to as the wintertime mean NAO index. The dashed lines denote ±0.5 standard deviation. Positive (negative) NAO winters are defined when this index exceed +0.5 (−0.5) standard deviation.

Before doing so, it is useful to show the phase relationships between the NAO pattern and various fields such as the background jet stream, the meridional potential vorticity gradient (PV_y), and the KE on the synoptic-scale (K^2) and intraseasonal-scale (K^1) window. Figure 2 displays the spatial patterns of zonal wind anomaly (U), PV_y, K^2, and K^1 at 300 hPa regressed onto the daily NAO index. The regressed U exhibits a tripolar pattern of almost zonally oriented anomalies, with a positive band from 45° to 65°N and negative bands to its south and north (Fig. 2a). This indicates that North Atlantic midlatitude jet stream is intensified (weakened) and shifts northward (southward) for the NAO^+ (NAO^-), consistent with previous findings (e.g., Luo et al. 2018). There is a high spatial coincidence between the regressed patterns of PV_y and U (Figs. 2a,b). According to the equivalent barotropic PV model developed by Luo et al. (2018), enhanced (reduced) PV_y is indicative of enhanced (reduced) energy dispersion and reduced (enhanced) nonlinearity. The close linkage between the two properties indicates that the NAO^+ is associated with an enhanced energy dispersion and hence reduced nonlinearity due to the intensified and northward shifted jet stream. The opposite is true for the NAO^-. In section 4, we will show that the dispersion–nonlinearity relation in the life cycle of NAO events is not as simple as the one predicted by the barotropic model, especially when considering their interannual regimes.

Changes in jet strength and position alter the atmospheric baroclinicity and thus impact the storm-track eddy activity. As can be seen from Fig. 2c, the NAO^+ (NAO^-) is associated with an increase (decrease) of K^2 along the band where the regressed U is anomalously strong (weak), especially in the eastern Atlantic sector. Similar in-phase relation between the Atlantic storm-track eddy activity and the daily NAO index has been reported in previous studies (Lorenz and Hartmann 2003; Rivière and Orlanski 2007; Castanheira and Marques 2019). This contrasts with that for the intraseasonal variability where K^1 is found to be negatively correlated with the daily NAO index over the most of the midlatitude and high-latitude North Atlantic (Fig. 2d), indicating that the NAO^- is associated with enhanced intraseasonal variability over the North Atlantic, and vice versa, in agreement with previous findings (Rennert and Wallace 2009; Ma and Liang 2023). This is not surprising because the NAO^- is characterized by a strong meandering jet stream, whereas the jet stream takes a less meandering path for the NAO^+ (Benedict et al. 2004). Since both phases vary on the intraseasonal time scale, the meandering jet stream for the NAO^- generally contains more intraseasonal KE than its NAO^+ counterpart.

The above results based on regression analysis are consistent with our previous knowledge about the fundamental aspects of the NAO. However, the regression method alone cannot discriminate the asymmetric features embedded in the growth and decay of the two phases as well as their different characteristics on the interannual time scale. In the following, we conduct lagged composite analyses to fulfill the purpose.

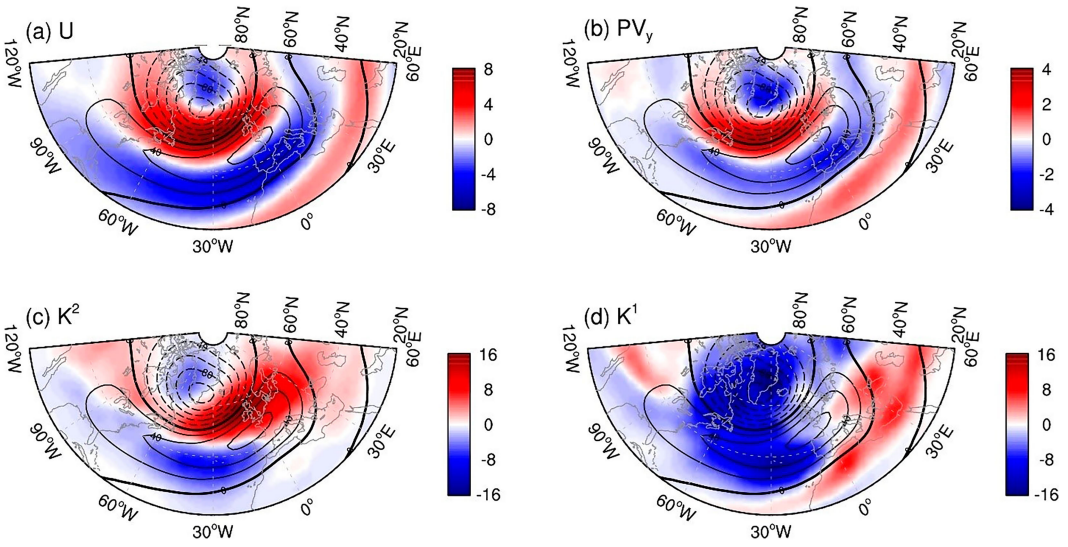

FIG. 2. Spatial patterns of (a) zonal wind (U; unit: m s^{-1}), (b) PV$_y$ (unit: 10^{-13} K m^2 kg^{-1} s^{-1}), (c) K^2 (unit: m^2 s^{-2}), and (d) K^1 (unit: m^2 s^{-2}) at 300 hPa regressed onto the daily NAO index. Superimposed in black contours is the regressed pattern of geopotential height at 300 hPa. The contour interval (CI) is 20 gpm. Solid (dashed) thin contours denote positive (negative) values, and zero contours are thick and solid.

b. *Lagged composite results*

1) STATISTICS

Figure 3 shows the time series of the daily NAO index for individual (thin gray lines) and composite (i.e., the multievent average at each lag day; thick lines) NAO events. During the 141 winters from December 1871 to February 2012, there are 254 NAO$^+$ and 271 NAO$^-$ events according to our identification procedure. On average, the NAO$^+$ (NAO$^-$) events have an *e*-folding time scale of about 8 (9) days and peak amplitude of 1.72 (−1.89) (Table 1). This indicates that the NAO$^-$ events tend to have a slightly more persistent lifespan and stronger amplitude than the NAO$^+$ events, consistent with previous results (e.g., Woollings et al. 2010; Luo et al. 2018). In contrast to the moderate asymmetries of persistence and amplitude between the two phases, the NAO events exhibit a clear distinction between different interannual regimes. As can be seen from Table 1, the number of NAO$^+_{PW}$ is more than twice than that of NAO$^+_{NW}$. The *e*-folding time scale of the composite NAO$^+_{PW}$ is about 10 days, whereas that of the NAO$^+_{NW}$ is only about 6 days. Besides, the peak amplitudes of the composite NAO$^+_{PW}$ and NAO$^+_{NW}$ are 2.05 and 1.25, respectively. Therefore, on average, NAO$^+$ occurs more frequently, and is more persistent and stronger during positive NAO winters than in negative NAO winters. Similarly, NAO$^-$ is more frequent, persistent, and stronger in negative NAO winters (cf. the statistics of NAO$^-_{PW}$ and NAO$^-_{NW}$ in Table 1). These results imply that the interannual variation of the wintertime mean NAO index is closely related to the ensemble mean of NAO events that are essentially occurring on the intraseasonal time scale, in agreement with previous studies by Johnson et al. (2008) and Luo et al. (2011, 2012). That is, the positive interannual NAO regime is dominant by higher (lower) occurrence frequency of NAO$^+$ (NAO$^-$) events, with more (less) persistent lifespan and enhanced (reduced) intensity than their mean condition (i.e., composite including all winters). In contrast, the negative interannual NAO regime is dominant by higher (lower) frequency of occurrence of NAO$^-$ (NAO$^+$) events, with more (less) persistent lifespan and enhanced (reduced) intensity than their mean condition.

2) TEMPORAL EVOLUTION OF THE NAO PATTERN

Figures 4a and 4d respectively show the time-evolving spatial structure of the 300-hPa geopotential height anomaly (color shading) for the composite NAO$^+$ and NAO$^-$ events in all winters. Noticeable differences can be seen between the life cycles of the two phases. For the NAO$^+$ events (Fig. 4a), a weak negative geopotential height anomaly appears over the east coast of North America about one week before the onset day. This anomaly develops, propagates downstream and forms the northern lobe of the NAO$^+$ pattern over Greenland. After the onset day, the negative anomaly decays rapidly and moves eastward. In contrast, the onset of the NAO$^-$ pattern is associated with the westward propagation and intensification of a positive anomaly that first appears east of Greenland (Fig. 5a). These asymmetric features of two NAO phases are consistent with previous composite analyses (e.g., Feldstein 2003; Jia et al. 2007; Luo et al. 2018).

To see the interannual variability, we show in Figs. 4b, 4c and 5b, 5c the lagged composites of NAO$^+$ and NAO$^-$ events, respectively, in positive and negative NAO winters. As expected, the amplitude and persistence of the NAO$^+_{PW}$ (NAO$^-_{NW}$) dipole are noticeably larger and longer than those of the NAO$^+_{NW}$ (NAO$^-_{PW}$). Take the NAO$^+$, for example, significant negative anomaly appears around lag −6 days in the

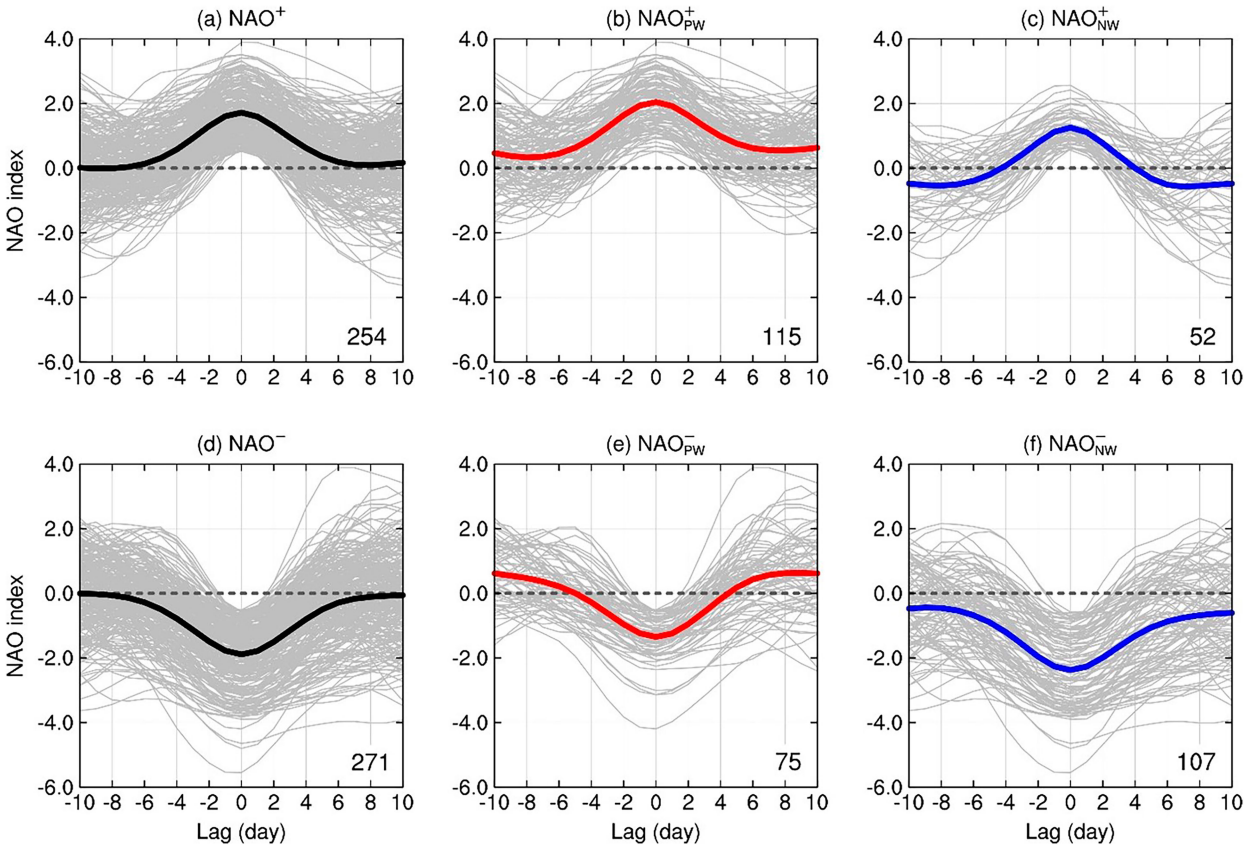

FIG. 3. Time series of the daily NAO index for the individual (a) NAO^+, (b) NAO^+_{PW}, (c) NAO^+_{NW}, (d) NAO^-, (e) NAO^-_{PW}, and (f) NAO^-_{NW} events (gray thin lines). Thick lines denote their respective composite means. The number of events for each group is denoted at the bottom-right corner in each subplot.

positive NAO winters, much earlier than that in the mean condition (cf. Figs. 4a,b). Also, the negative anomaly persists much longer than that in the mean condition. In contrast, in the NAO negative winters, the negative anomaly does not seem to be fully established until lag −2 days, before which the region is instead occupied by a positive anomaly (Fig. 4c). The negative anomaly decays much faster than in its mean condition, and is replaced by a positive anomaly at lag +6 days (cf. Figs. 4a,c). Similarly, from Figs. 5b and 5c, one immediately sees that the growth and decay of the NAO^- dipole structure are much more persistent and intensified during the negative NAO winters than those in the positive NAO winters.

As mentioned in the previous subsection, the temporal evolution of the NAO events is closely related to the strength and position of the North Atlantic midlatitude jet stream. The lagged composite U (black contours in Figs. 4a and 5a) shows that as the dipole pattern grows, the midlatitude jet stream gets strengthened (weakened) and shifts northward (southward) for the NAO^+ (NAO^-), consistent with previous findings (e.g., Woollings et al. 2008; Luo et al. 2018). The reverse is true for the decay stage of the dipole pattern. Regarding the interannual regimes, the jet stream is stronger for the NAO^+_{PW} than for the NAO^+_{NW} (black contours in Figs. 4b,c), and is weaker for the NAO^-_{NW} than for the NAO^-_{PW} (black contours in Figs. 5b,c).

TABLE 1. Statistics of the NAO events.

Type	Meaning	No. of events	Peak amplitude	*e*-folding time scale (days)
NAO^+	Positive NAO events in all winters	254	1.72	8
NAO^+_{PW}	Positive NAO events in positive NAO winters	115	2.05	10
NAO^-_{PW}	Negative NAO events in positive NAO winters	52	1.25	6
NAO^-	Negative NAO events in all winters	271	−1.89	9
NAO^+_{NW}	Positive NAO events in negative NAO winters	75	−1.35	7
NAO^-_{NW}	Negative NAO events in negative NAO winters	107	−2.37	11

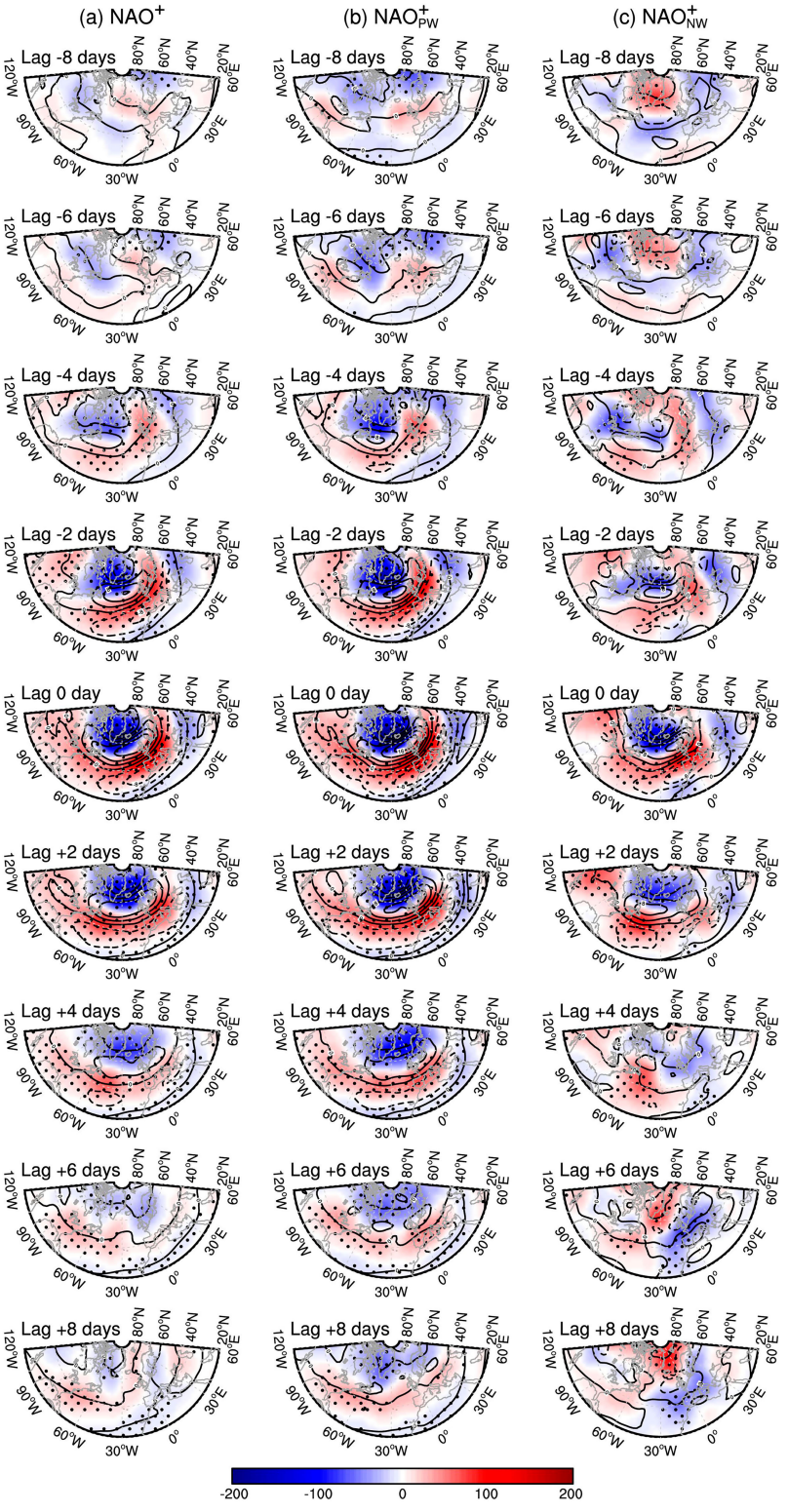

FIG. 4. Time-evolution spatial patterns of geopotential height anomalies (color shading; unit: gpm) and zonal wind anomalies (black contours; CI: 4 m s^{-1}) at 300 hPa for (a) NAO^+, (b) NAO^+_{PW}, and (c) NAO^+_{NW} events. Stippled are regions where the composite geopotential height anomalies are significant at the 90% confidence level based on the Student's *t* test.

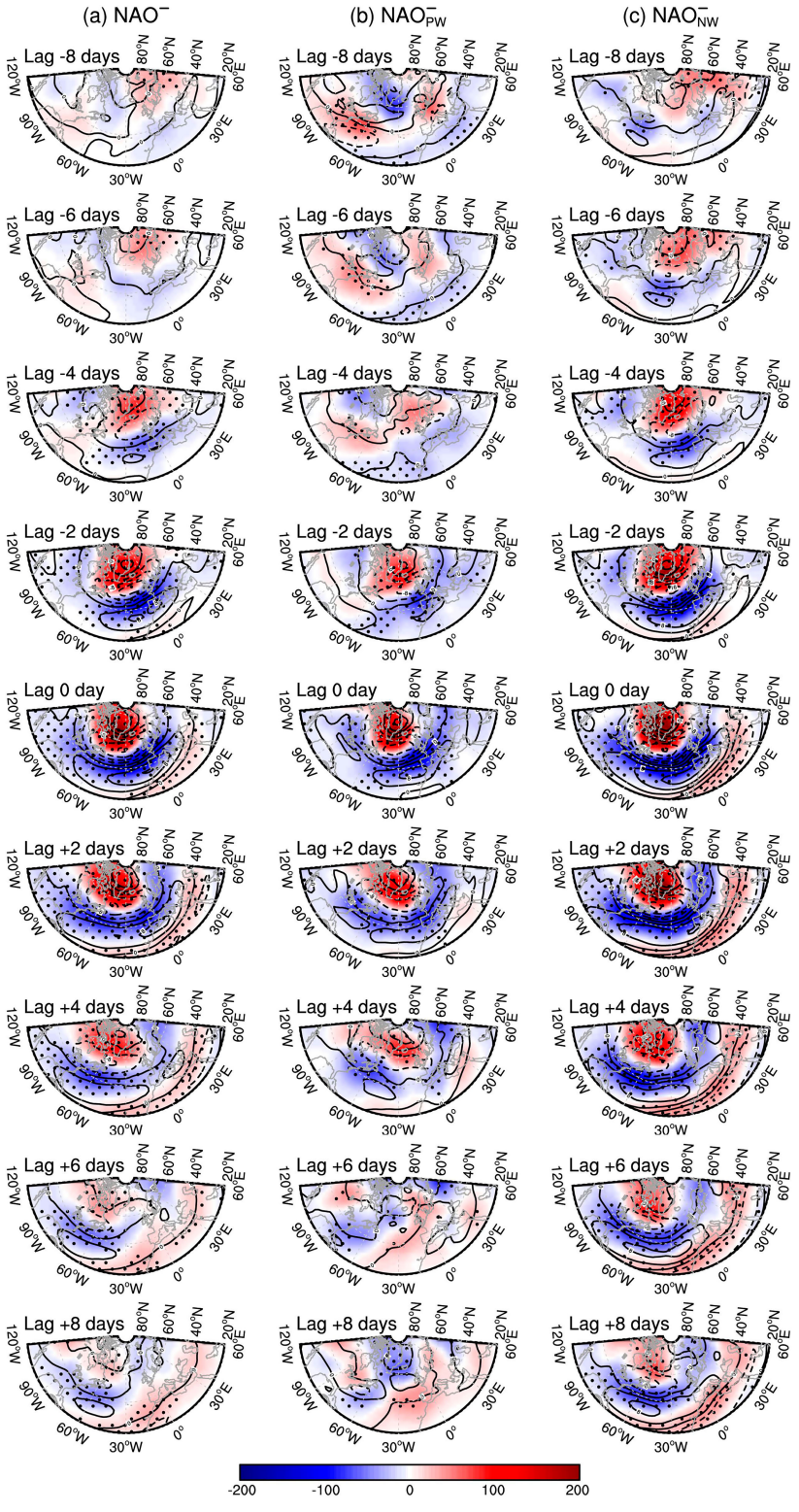

FIG. 5. As in Fig. 4, but for (a) NAO^-, (b) NAO^-_{PW}, and (c) NAO^-_{NW}.

3) SYNOPTIC- AND INTRASEASONAL-SCALE KINETIC ENERGY

Figures 6 and 7 displays the lagged composite of K^1 (color shadings) and K^2 (black contours) at 300 hPa for the NAO^+, NAO^-, and their interannual regimes. When considering composite through all winters, K^2 is more zonally expanded and intensified for the NAO^+ than the NAO^- (see lag −4 to +4 days in Figs. 6a and 5d), and has an in-phase relation with the background U (black contours in Figs. 4a,d), consistent with the regression result. However, on the interannual time scale, the storm-track eddy activity does not exhibit a simple positive correlation with the jet strength. For example, K^2 is significantly larger for the NAO^+_{NW} just prior to the onset day (see lag −2 days in Figs. 6b and 5c), during which the jet stream has a weaker intensity (Figs. 4b,c). In contrast, during the decay stage of the NAO^- (see lag 0 to +4 days in Figs. 6e and 5f), K^2 is significantly stronger for the NAO^-_{PW} than the NAO^-_{NW}.

The phase- and regime-dependent features of the NAO-related storm-track eddy activity can be better seen in the domain-averaged time series of K^2 over the area of 37°–70°N, 60°W–0° (Figs. 8a,b). The area, similar to the one defined in Barnes and Hartmann (2010), is denoted as the "NAO region" throughout the paper. We find that our results are not sensitive to small changes in domain size due to the coherent structures of the physical processes discussed in this study. The area-mean K^2 from lag −5 to +7 days (black lines in Figs. 8a,b) appears larger for the NAO^+ than the NAO^-, which is statistically significant at the 90% confidence level for a two-sided Student's t test. In particular, the onset of NAO^+ is preceded by a significant increase of synoptic eddy activity (lag −5 to −1 days), while the level of K^2 remains quite low prior to the onset of NAO^-. The interannual composites of K^2 exhibit more complex variations (red and blue lines in Figs. 8a,b). Although the differences between positive and negative NAO winters fall below the 90% confidence level at many lags (possibly due to a decreased sample of events used in the interannual composites), some noticeable aspects stand out: 1) there is a significant increase of K^2 at the early stage of NAO^+_{PW} (see lag −10 to −8 days in Fig. 8a) compared to that of NAO^+_{NW}; 2) K^2 increases sharply in the segment of lag −6 to −1 days for the NAO^+_{NW} and even exceeds its counterpart of the NAO^+_{PW} before the onset day (Fig. 8a); 3) K^2 is overall larger during the life cycle of NAO^-_{PW} than that of NAO^-_{NW}, especially in the decay stage (Fig. 8b).

The temporal evolution of K^1 is more coherent than K^2. A glance of its time-evolving spatial patterns (color shading in Fig. 6) reveals that K^1 has stronger loadings in the Atlantic sector from lag −2 to +6 days for the NAO^- than the NAO^+, consistent with the regression result. On the interannual time scale, the NAO^+ has stronger K^1 during the negative NAO winters than the positive NAO winters, especially in the segment of lag −2 to +6 days (cf. the NAO^+_{PW} and NAO^+_{NW} composites in Figs. 6 and 8c). Regarding the NAO^- case, during the peak period from lag −2 to +1 days, K^1 is stronger in amplitude for the NAO^-_{PW} than the NAO^-_{NW}, whereas the reverse occurs for the early and decay stages (Figs. 7 and 8d). It is interesting to note that, during the decay stage, K^1 can be even larger for the NAO^+_{NW} than for the NAO^-_{NW} (blue lines in Figs. 8c,d), indicating that the relation between K^1 and the phase of NAO can be different in the two interannual regimes.

The above results indicate that the relation between the NAO flow and transient eddy activity may not be as unambiguous as those suggested in previous studies (Lorenz and Hartmann 2003; Barnes and Hartmann 2010; Luo et al. 2015). Luo et al. (2015) noted a positive correlation between the NAO^- amplitude and the synoptic-scale eddy KE in their barotropic model, which seems inconsistent with the observation that the NAO^+ is associated with anomalously high synoptic eddy activity level in the NAO region. Another mechanism proposed by Lorenz and Hartmann (2003), which states that synoptic eddies and the NAO-related zonal wind anomaly reinforce each other, seems to be more in agreement with the observations. Barnes and Hartmann (2010) argued that the enhanced synoptic eddies during NAO^+ do not feed back to the anomalous NAO flow effectively due to their extended downstream dispersion by the strong jet stream. Conversely, the weak jet stream during NAO^- allows more synoptic eddies to break in the NAO region, leading to efficient eddy feedback to the NAO flow. Nevertheless, these previous studies did not address the interannual regimes of the NAO events, which should be considered separately due to their distinct dynamical characteristics as mentioned earlier. In section 4, we will show that the eddy forcing processes, in terms of inverse cascading process, are highly phase and regime dependent.

4. Dynamical analysis

In the previous section, we have shown that the growth and decay of the two phases of the NAO are characterized by distinct KE evolution on both intraseasonal and synoptic time scales. Further distinction is revealed by separating the events into different interannual regimes, i.e., positive NAO winters and negative NAO winters. In this section, we will identify the sources and sinks of K^1 during the life cycles of the events within the three-scale energetics framework as introduced in section 2a, with a focus on the asymmetric characteristics of energetic processes between different phases and regimes. The equation for the K^1 tendency can be written symbolically as

$$\frac{\partial K^1}{\partial t} = \Gamma_K^{0\to1} + \Gamma_K^{2\to1} + B^1 + (D_K^1 + \Pi^1) + R_K^1, \tag{10}$$

where we have omitted the terms $\Gamma_K^{1\to1}$ and $\Gamma_K^{0\oplus2\to1}$ due to the following reasons. First, $\Gamma_K^{0\oplus2\to1}$ is negligibly small compared to $\Gamma_K^{0\to1}$ and $\Gamma_K^{2\to1}$ (Fig. 9). Second, the small but nonnegligible $\Gamma_K^{1\to1}$ does not show a significant interannual variation and therefore cannot explain the distinct K^1 variation regarding the interannual regimes of the NAO (Fig. 9).

The above budget equation shows that the temporal evolution of the K^1 is controlled by five processes: 1) $\Gamma_K^{0\to1}$: the

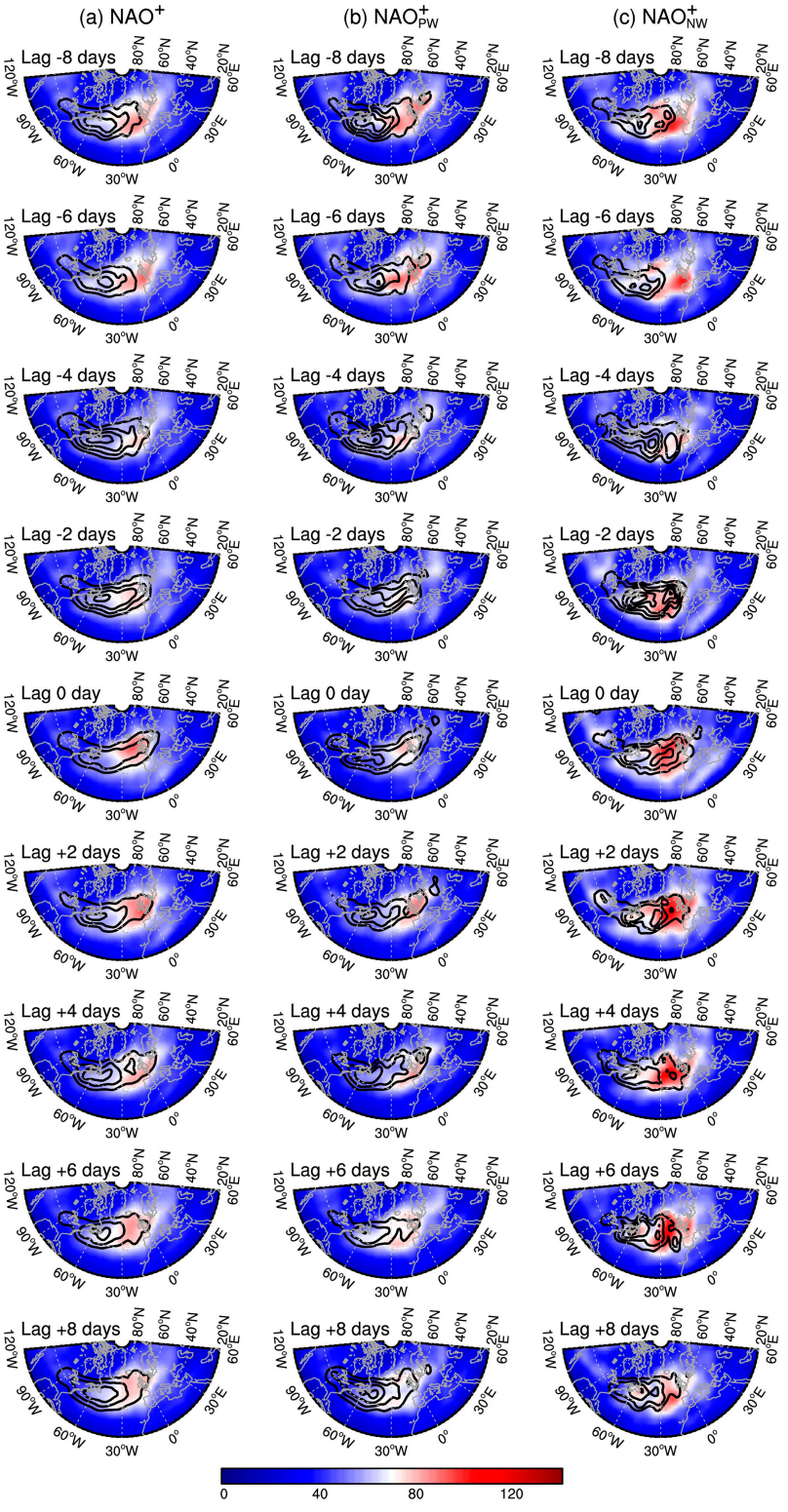

FIG. 6. Time-evolution spatial patterns of the vertically averaged (1000–100 hPa) K^1 (color shading; unit: $m^2\ s^{-2}$) and K^2 (black contours; CI: 10 $m^2\ s^{-2}$ starting from 40 $m^2\ s^{-2}$) for (a) NAO^+, (b) NAO^+_{PW}, and (c) NAO^+_{NW}.

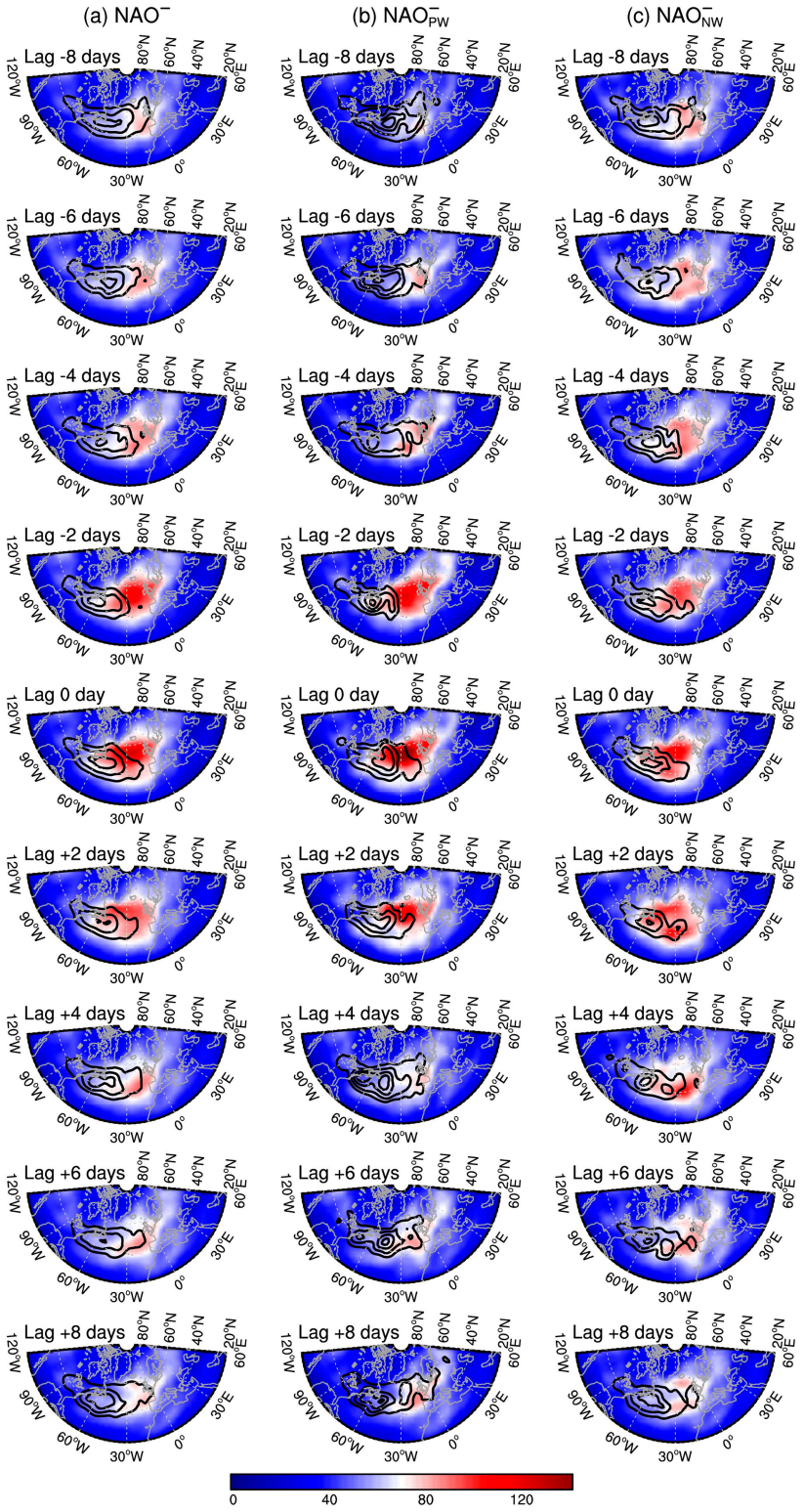

FIG. 7. As in Fig. 6, but for (a) NAO^-, (b) NAO^-_{PW}, and (c) NAO^-_{NW}.

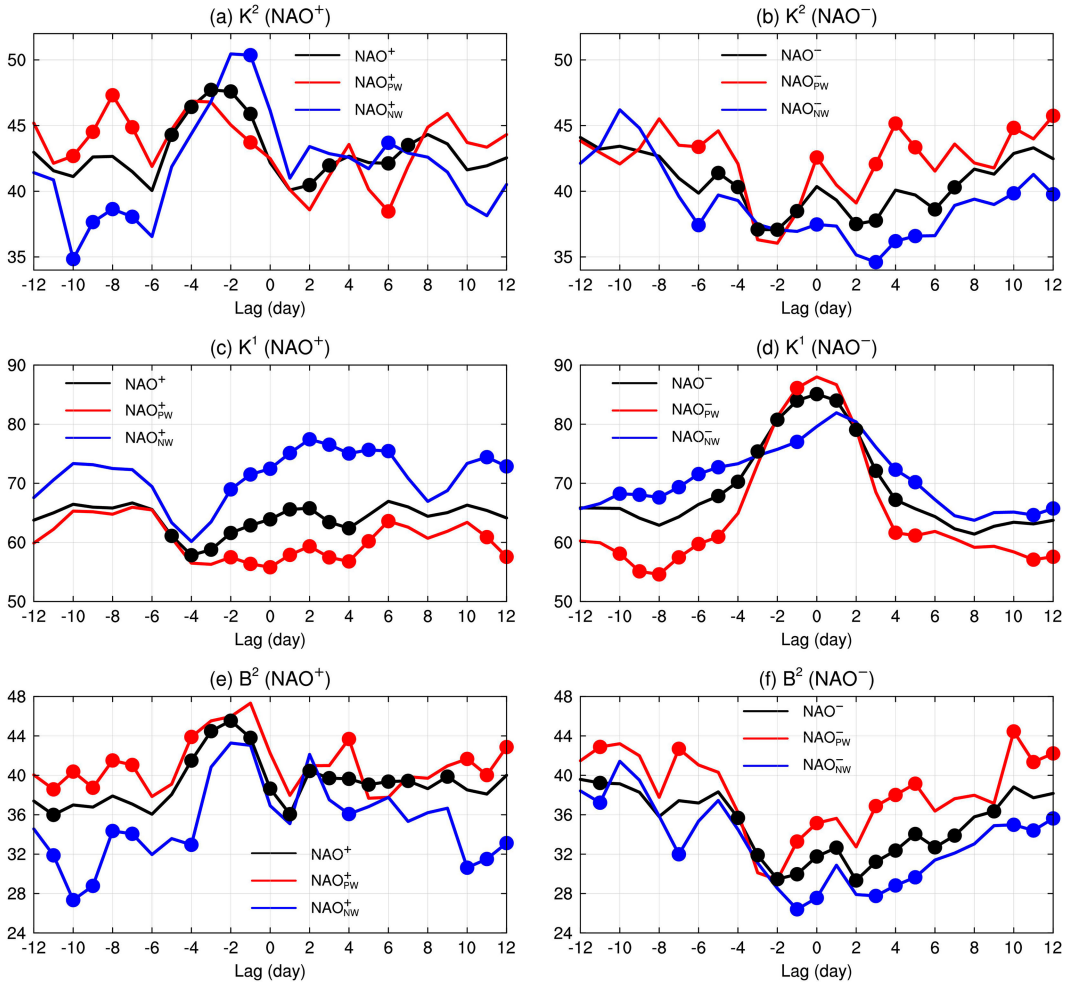

FIG. 8. Composite daily time series of the volume-mean K^2 (unit: $m^2\ s^{-2}$) for (a) NAO^+ and (b) NAO^-. The volume averaging is taken over the area of 37°–70°N, 60°W–0° (referred to as the NAO region in this paper) and vertical layers from 1000 to 100 hPa. The black, red, and blue lines in (a) stand for the composite of all NAO^+ events, the NAO^+_{PW} events, and the NAO^+_{NW} events, respectively, whereas those in (b) stand for the composite of all NAO^- events, the NAO^-_{PW} events, and the NAO^-_{NW} events, respectively. The black dots in (a) and (b) indicate that the differences of K^2 between the NAO^+ and NAO^- are statistically significant at the 90% confidence level based on the two-sided Student's t test. The red and blue dots in (a) indicate that the differences of K^2 between the NAO^+_{PW} and NAO^+_{NW} are statistically significant at the 90% confidence level, whereas those in (b) indicate that the differences of K^2 between the NAO^-_{PW} and NAO^-_{NW} are statistically significant at the 90% confidence level. (c),(d) As in (a) and (b), but for K^1 (unit: $m^2\ s^{-2}$). (e),(f) As in (a) and (b), but for B^2 (unit: $10^{-5}\ m^2\ s^{-3}$).

barotropic canonical transfer from the background mean flow to the intraseasonal-scale flow (positive means a transfer of KE from the mean flow to the intraseasonal flow, and vice versa); 2) $\Gamma_K^{2\to1}$: the barotropic canonical transfer from the synoptic transients to the intraseasonal-scale flow (positive means a transfer of KE from the synoptic transients to the intraseasonal flow, and vice versa); 3) B^1: baroclinic energy conversion between APE and K^1 (positive means a conversion from APE to K^1, and vice versa); 4) $D_K^1 + \Pi^1$: nonlocal dispersion of K^1 due to advection and geopotential flux (positive means inward energy fluxes from surrounding regions, and vice versa); and 5) R_K^1: dissipation. In the following, we will diagnose these terms to unravel the energetics underlying the two phases of the NAO events (section 4a) and their interannual regimes (section 4b).

a. NAO^+ and NAO^- composites

The black lines in Fig. 10 depict the temporal evolutions of the five terms on the right-hand side of Eq. (10) averaged over the NAO region during the life cycles of the composite NAO^+ and NAO^- events though all winters. It can be seen that $\Gamma_K^{0\to1}$ remains relatively small before the onset of NAO^+ but reaches its peak at lag +1 days (Figs. 10a and 11a). This could explain why there is a moderate peak of K^1 after the onset of NAO^+. In contrast, the onset of NAO^- is preceded by an increase of $\Gamma_K^{0\to1}$ from lag −6 to −1 days (Fig. 10b). After

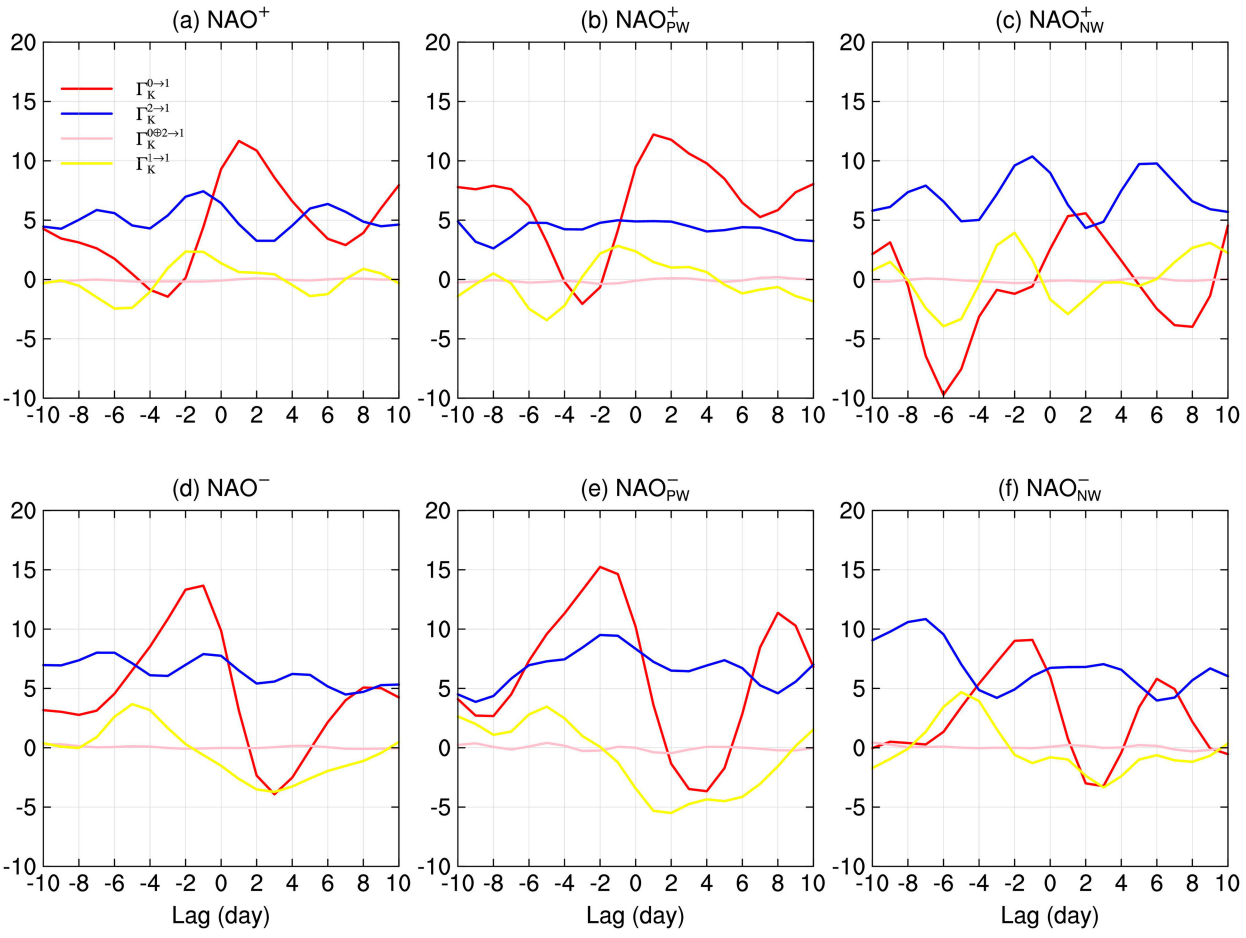

FIG. 9. Composite daily time series of the volume-mean of $\Gamma_K^{0\to1}$ (red), $\Gamma_K^{2\to1}$ (blue), $\Gamma_K^{0\oplus2\to1}$ (pink), and $\Gamma_K^{1\to1}$ (yellow) for (a) NAO^+, (b) NAO^+_{PW}, (c) NAO^+_{NW}, (d) NAO^-, (e) NAO^-_{PW}, and (f) NAO^-_{NW}. All terms are in units of 10^{-5} m^2 s^{-3}. As in Fig. 8, the volume averaging is taken over the NAO region and vertical layers from 1000 to 100 hPa.

reaching its peak, $\Gamma_K^{0\to1}$ decreases sharply and even changes its sign to negative at about lag +3 days. The spatial pattern of $\Gamma_K^{0\to1}$ reveals a coherent positive pool in the NAO region prior to the onset of NAO^- (Fig. 12a). These results indicate that barotropic instability plays an important role in energizing the onset of NAO^- by transferring KE from the background jet stream to the intraseasonal NAO flow, consistent with previous study by Ma and Liang (2023).

Compared to the large amplitude of $\Gamma_K^{0\to1}$, $\Gamma_K^{2\to1}$ shows a relatively weak oscillation during the life cycle of NAO events (black lines in Figs. 10c,d; see also Fig. 9). It should be mentioned that the relative smaller amplitude of $\Gamma_K^{2\to1}$ as compared to $\Gamma_K^{0\to1}$ during most of the lag days is not likely due to the cancellation between different events. This is confirmed when looking at the variance of two terms (Fig. S1 in the online supplementary material), which shows that the standard deviation of $\Gamma_K^{0\to1}$ is also larger than that of $\Gamma_K^{2\to1}$. The positive sign of $\Gamma_K^{2\to1}$ indicates that synoptic eddies indeed act to feed the lower-frequency NAO flow via inverse cascades. From the spatial pattern, one can see that $\Gamma_K^{2\to1}$ is mainly distributed in the downstream of the NAO region (Figs. 13 and 14). The time sequence exhibits oscillatory behavior during the life cycles of NAO^+ and NAO^-, with a moderate peak (below the 90% confidence level) at lag −1 days for both phases (Figs. 10c,d). Significant difference between the two phases exists in the segment of lag −12 to −6 days during which $\Gamma_K^{2\to1}$ is significantly larger for the NAO^- than the NAO^+. It should be noted that neither K^1 nor K^2 during this time segment shows a significant difference between the two phases. As will be shown in the next subsection, the overall insignificant eddy forcing strength, in terms of inverse cascades of KE, in the composites through all winters, is due to a large offset of this process between the two interannual regimes.

In addition to the above two source terms, baroclinic energy conversion (B^1) is another key source of K^1, especially during the decay stage of the event (black lines in Figs. 10e,f). This term maximizes over the western Atlantic basin and eastern North America, and is generally in larger amplitude during the life cycle of the NAO^- than that of the NAO^+ over the NAO region (see Figs. 15 and 16). Note that positive B^1 is associated with the ascending of warm air and sink of

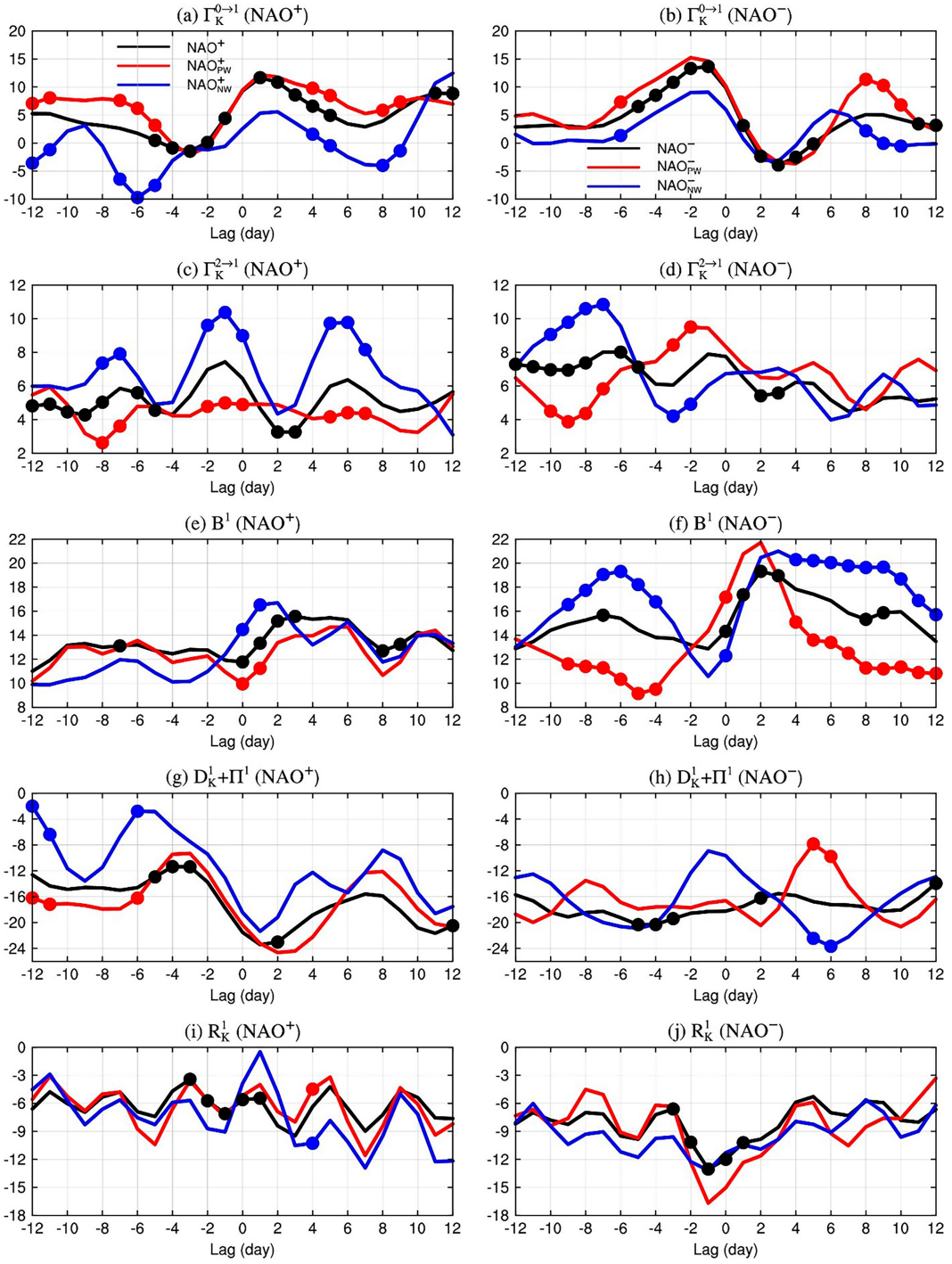

FIG. 10. As in Fig. 8, but for (a),(b) $\Gamma_K^{0\to1}$, (c),(d) $\Gamma_K^{2\to1}$, (e),(f) B^1, (g),(h) $D_K^1 + \Pi_K^1$, and (i),(j) R_K^1. The energy terms are all in units of 10^{-5} m^2 s^{-3}.

cold air anomalies on the intraseasonal time scale. This suggests that the baroclinic energy conversion associated with the slow changes of the overturning circulation is an important energy source that maintains the NAO$^-$ against dissipation. The positive B^1 also contributes to the K^1 growth in the decay stage of the NAO$^+$, but with a much smaller amplitude compared to that of the NAO$^-$.

Nonlocal energy dispersion ($D_K^1 + \Pi^1$) and dissipation (R_K^1) are the two dominant sinks of K^1 over the NAO region (Figs. 10g–j). Due to the high variances of these two processes,

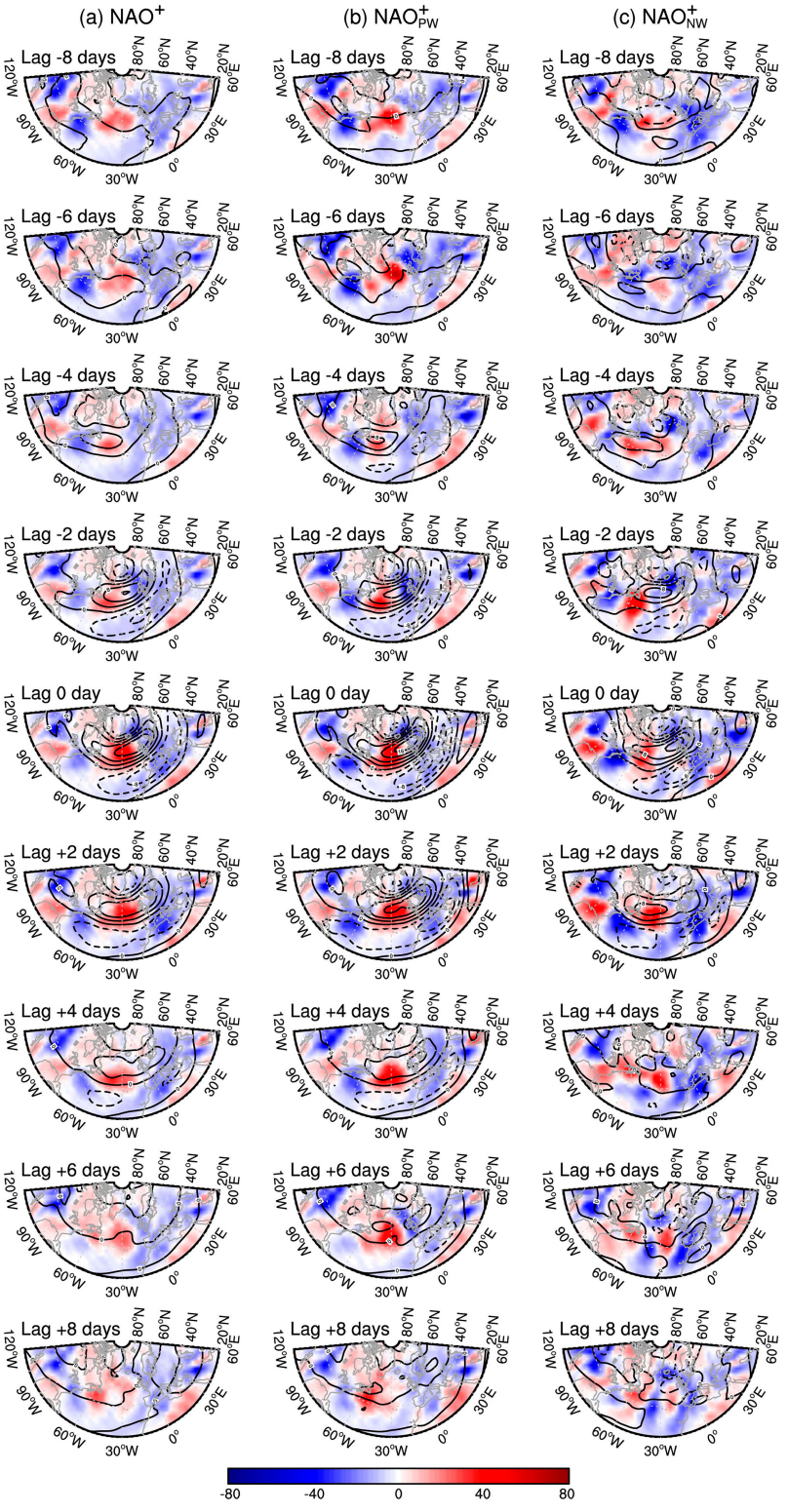

FIG. 11. Time-evolution spatial patterns of the vertically averaged (1000–100 hPa) $\Gamma_K^{0\to1}$ (color shading; unit: 10^{-5} m^2 s^{-3}) and zonal wind anomalies (black contours; CI: 4 m s^{-1}) at 300 hPa for (a) NAO$^+$, (b) NAO$^+_{\mathrm{PW}}$, and (c) NAO$^+_{\mathrm{NW}}$.

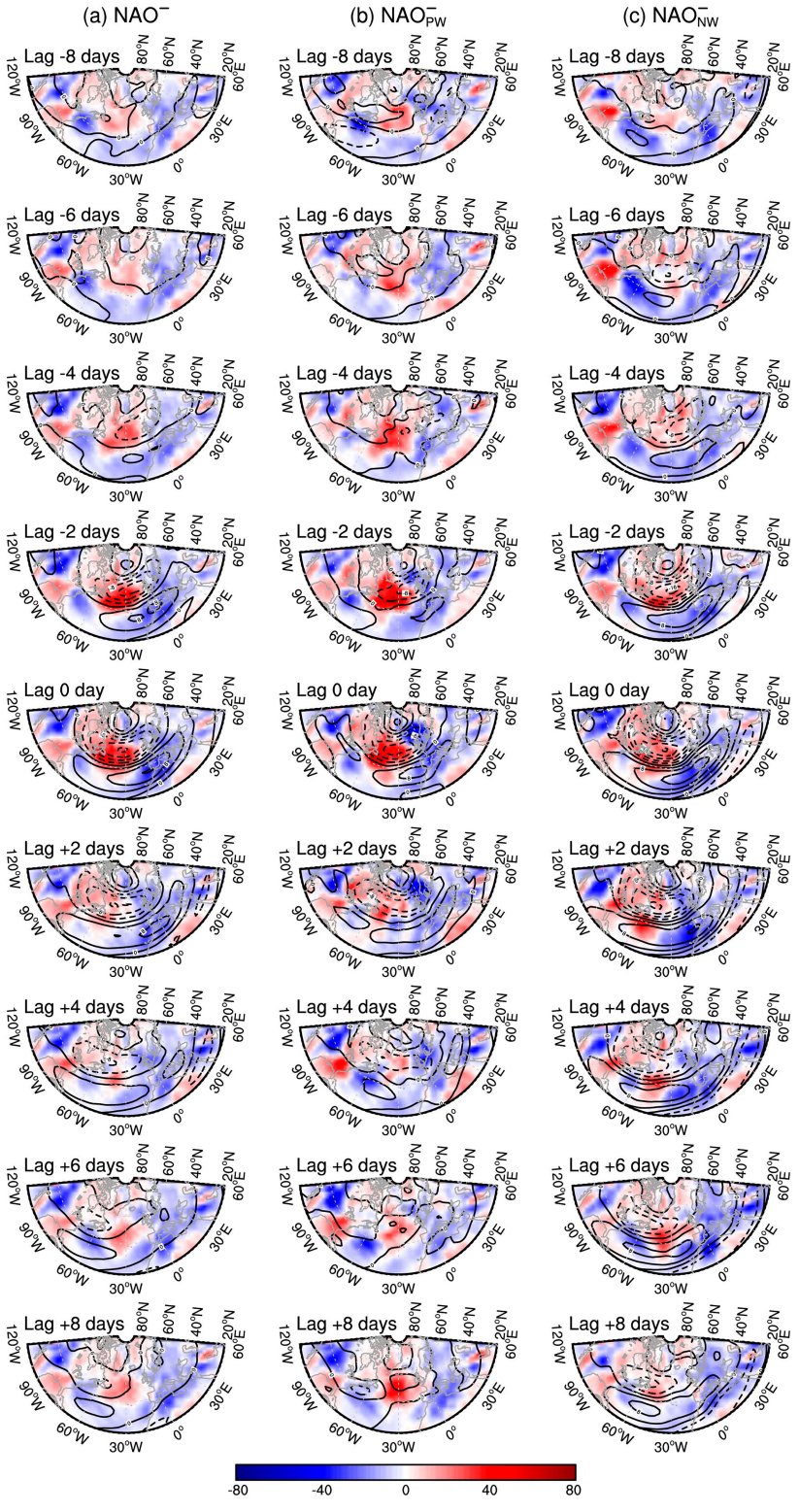

FIG. 12. As in Fig. 11, but for (a) NAO^-, (b) NAO^-_{PW}, and (c) NAO^-_{NW}.

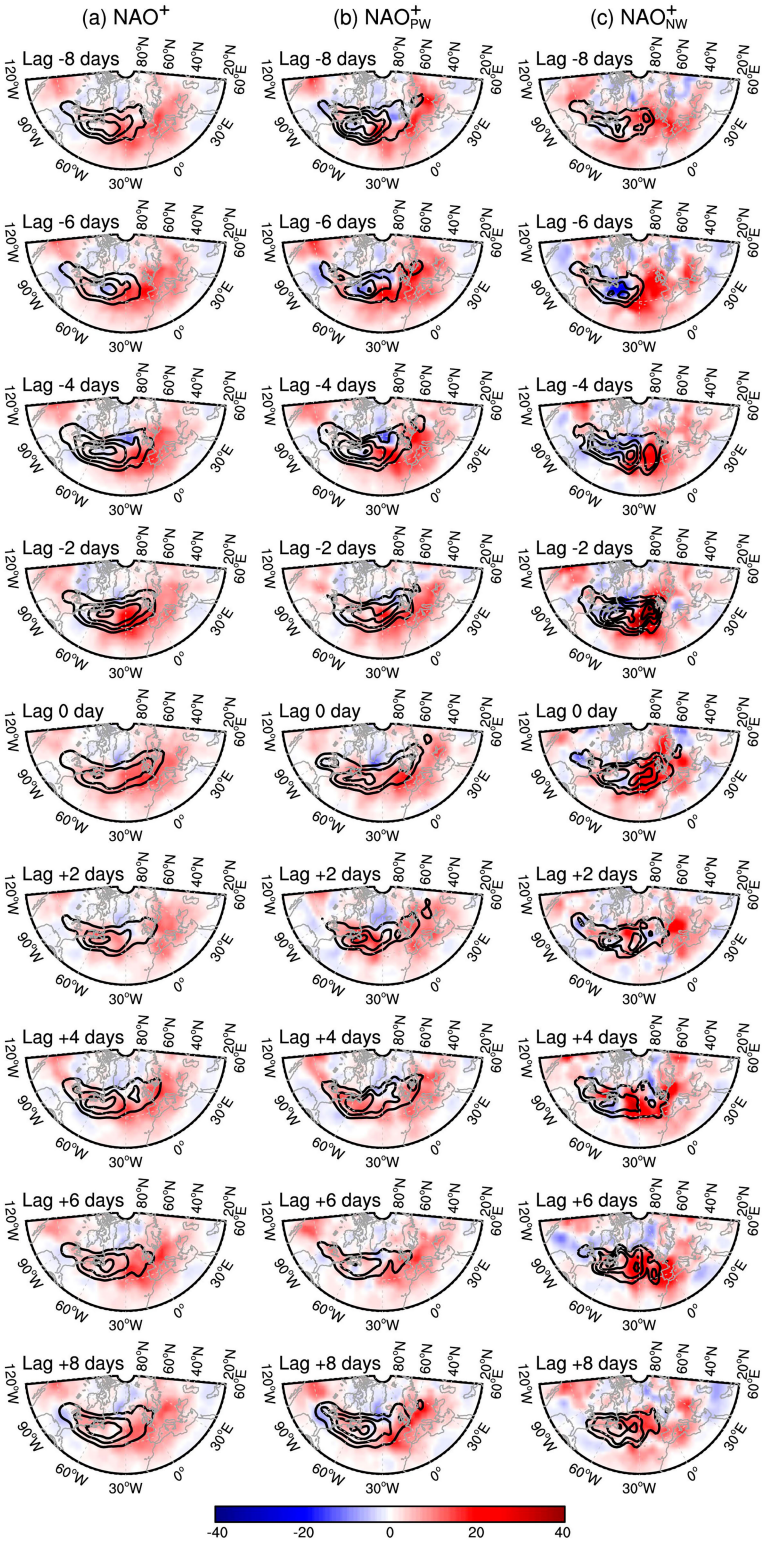

FIG. 13. Time-evolution spatial patterns of the vertically averaged (1000–100 hPa) $\Gamma_K^{2\to1}$ (color shading; unit: 10^{-5} m^2 s^{-3}) and K^2 (black contours; CI: 10 m^2 s^{-2} starting from 40 m^2 s^{-2}) for (a) NAO$^+$, (b) NAO$^+_{\mathrm{PW}}$, and (c) NAO$^+_{\mathrm{NW}}$.

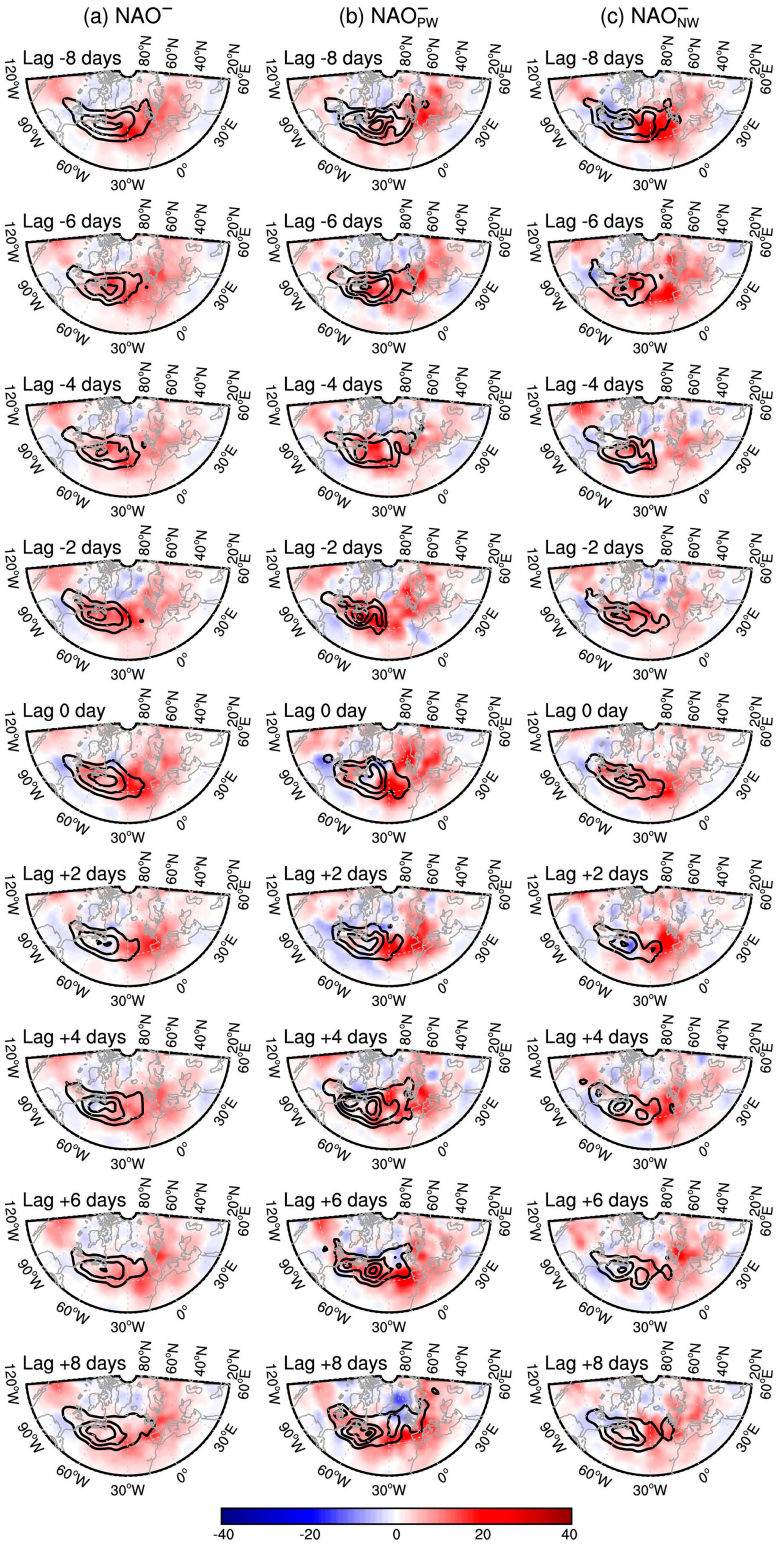

FIG. 14. As in Fig. 13, but for (a) NAO^-, (b) NAO^-_{PW}, and (c) NAO^-_{NW}.

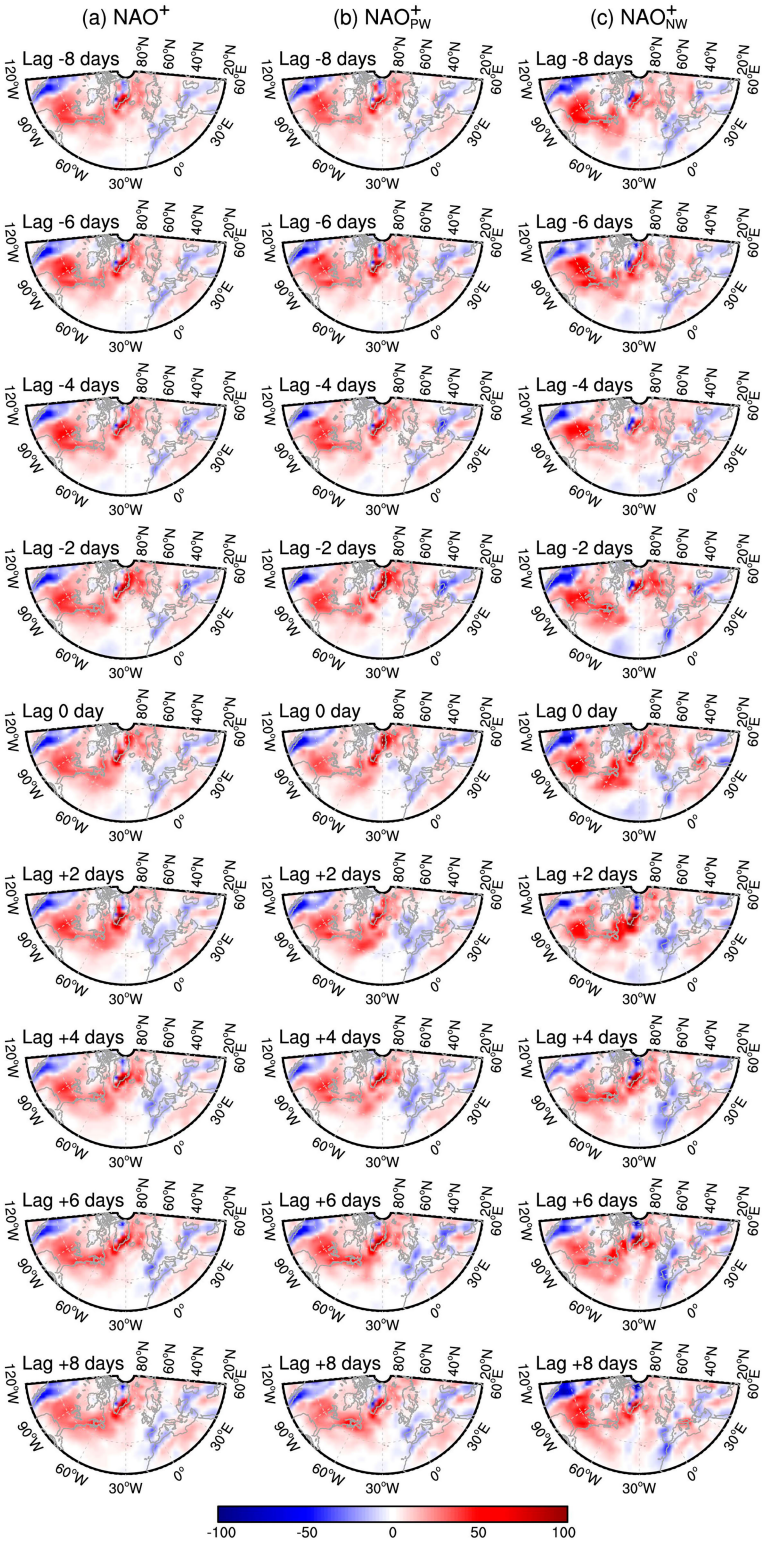

FIG. 15. Time-evolution spatial patterns of the vertically averaged (1000–100 hPa) B^1 (color shading; unit: 10^{-5} m^2 s^{-3}) for (a) NAO$^+$, (b) NAO$^+_{PW}$, and (c) NAO$^+_{NW}$.

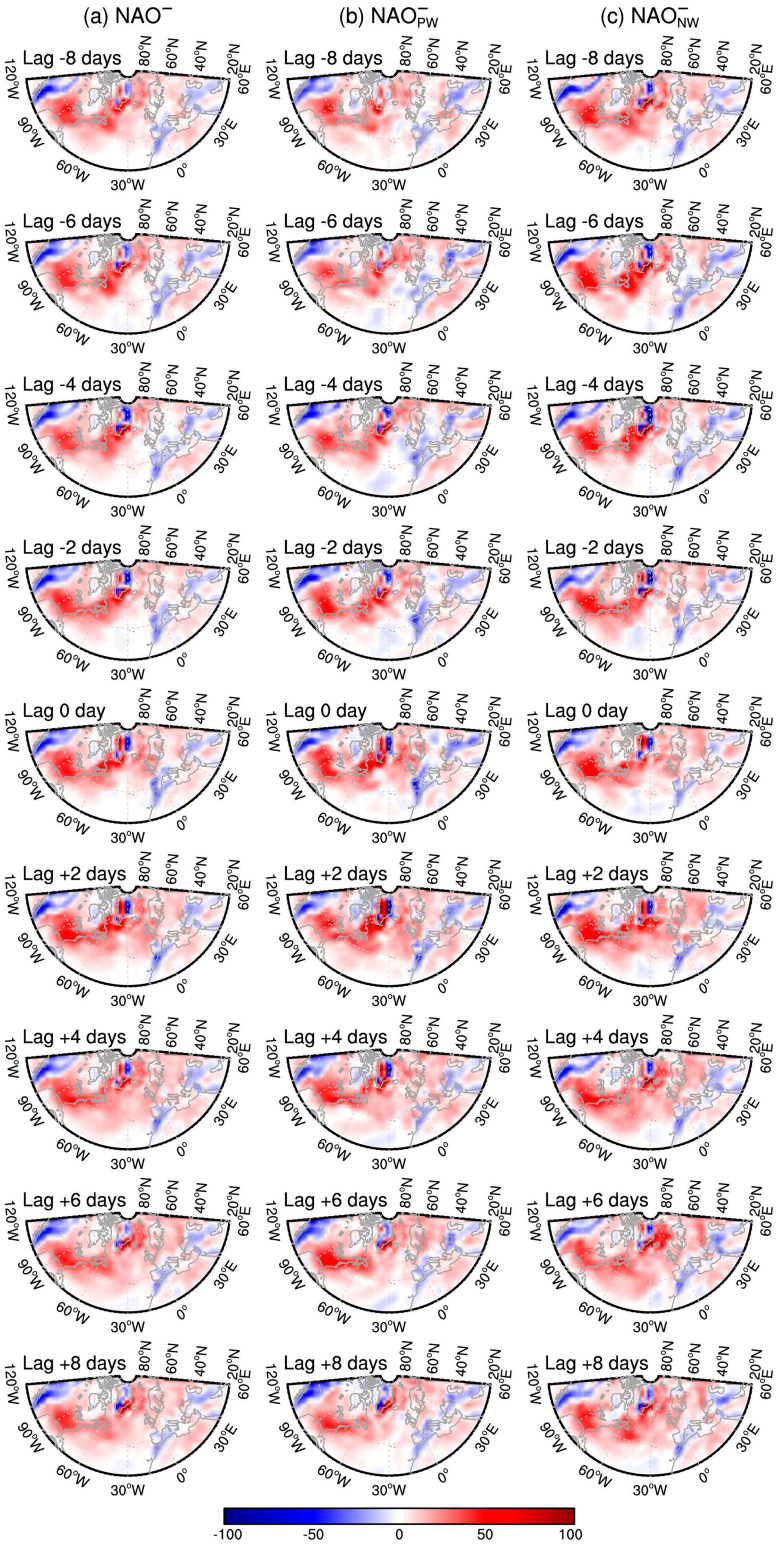

FIG. 16. As in Fig. 15, but for (a) NAO^-, (b) NAO^-_{PW}, and (c) NAO^-_{NW}.

their differences between the NAO^+ and NAO^- are not significant at the 90% confidence level for most lags. Nevertheless, some significant results are noticeable: 1) compared to the NAO^-, the outward energy flux for the NAO^+ is reduced in the growth stage and enhanced in the decay stage (Figs. 10g,h); 2) dissipation is generally more intensified for the NAO^- than for the NAO^+, especially during the segment from lag −3 to +1 day.

b. *Interannual regimes*

As mentioned above, the asymmetry of the interannual NAO regimes, in terms of the occurrence frequency, persistence, and amplitude of events as well as their associated energy reservoirs, can be more significant than that between the two phases of NAO, the latter of which has attracted much attention recently (Barnes and Hartmann 2010; Luo et al. 2018; Schmith et al. 2022; Zhao et al. 2023; Ma and Liang 2023). In the following, we investigate the dynamical processes responsible for the distinct features of the NAO events in the two interannual regimes.

Regarding the NAO^+ events, recall that K^1 over the NAO region is significantly larger for the NAO^+_{NW} than the NAO^+_{PW} (Fig. 8c). This feature cannot be explained by the interannual modulation of barotropic instability because $\Gamma_K^{0\to1}$ generally shows stronger value during the life cycle of the NAO^+_{PW} than that of the NAO^+_{NW} (red and blue lines in Fig. 10a). A striking difference exists between the inverse cascade processes ($\Gamma_K^{2\to1}$) of the two regimes (red and blue lines in Fig. 10c). For the NAO^+_{NW}, the strength of inverse cascades episodically rises and drops; three large and significant peaks occur at lag −7, −1, and +6 days, respectively. In contrast, the inverse cascade seems largely suppressed during the entire life cycle of the NAO^+_{PW}, which is likely due to the strong jet stream in the positive NAO winters so that the synoptic eddies do not have enough time to fully interact with the NAO^+ flow before they are advected out of the region. The above results indicate that the inverse cascade process plays an important role in the asymmetry between the K^1 variations during the NAO^+_{PW} and NAO^+_{NW} life cycle. That is, NAO^+_{NW} (NAO^+_{PW}) is associated with enhanced (reduced) inverse cascades from the synoptic eddies and thus intensified (weakened) KE on the intraseasonal time scale.

It is interesting to note that the strength of the inverse cascades does not seem to be positively correlated with the strength of the storm-track eddy KE reservoir. For example, there are enhanced (weakened) inverse cascades from the synoptic transients during the whole NAO^+_{NW} (NAO^+_{PW}) life cycle (Fig. 10c). In contrast, the K^2 level does not exhibit a noticeable enhancement during the life cycle of NAO^+_{NW} except in a short segment before the onset day (Fig. 8a). Since the dominant source of K^2 is the release of APE stored in the background jet stream via baroclinic instability, we plot the buoyancy conversion on the synoptic scale (denoted as B^2) in Figs. 8e and 8f. It can be seen that the strength of baroclinic generation is generally smaller during the life cycle of NAO^+_{NW} compared to NAO^+_{PW} (Fig. 8e). This seems to imply that the strength of the inverse cascading process is not proportional to the generation rate of synoptic transients. The underlying mechanism is more complex than what one might intuitively expect. A preliminary discussion from the perspective of the jet stream is presented in section 4c.

In addition to $\Gamma_K^{2\to1}$, B^1 also contributes to the anomalously large K^1 level for the NAO^+_{NW}, but its effect is only limited in a short segment between lag −1 and +3 days (Fig. 10e). With regard to the sink processes, nonlocal energy dispersion also exhibit a clear asymmetry between the NAO^+_{PW} and NAO^+_{NW} regimes (Fig. 10g). More K^1 is transported out of the NAO region for the NAO^+_{PW} due to the strengthened westerly jet stream. Inversely, K^1 tends to be accumulated in the NAO region due to reduced energy dispersion during the life cycle of NAO^+_{NW}. This suggests that nonlocal process also plays an important role in the asymmetry of NAO^+ between the two interannual regimes. The residue term R_K^1 displays oscillatory variation, with no significant differences between the two regimes. Besides, this term is generally smaller in amplitude than the nonlocal term.

The energetics of the NAO^- events in the two interannual regimes are more complex. As mentioned earlier, K^1 during the peak (early and decay) stage is more intensified for the NAO^-_{PW} (NAO^-_{NW}). Our goal here is to understand what physical processes control such time- and regime-dependent features. Similar to the NAO^+ case, $\Gamma_K^{0\to1}$ has a larger amplitude for the NAO^-_{PW} than for the NAO^-_{NW}, indicating that the background flow is more barotropically unstable during the positive NAO winters than the negative NAO winters. This can only explain the K^1 difference during the peak stage of the NAO^-_{PW} and NAO^-_{NW}. The temporal evolution of $\Gamma_K^{2\to1}$ and B^1 exhibits distinct (even opposite) evolutions during the life cycles of the NAO^-_{PW} and NAO^-_{NW}. It can be seen from Figs. 10d and 10f that $\Gamma_K^{2\to1}$ (B^1) is significantly larger from lag −10 (−9) to −7 (−4) days for the NAO^-_{NW} than the NAO^-_{PW}, whereas the reverse occurs during the segment from lag −5 (−2) to +1 (+2) days. This suggests that both the inverse cascades from synoptic eddies and baroclinic energy conversion are responsible for the excessive K^1 at the early (peak) stage of NAO^-_{NW} (NAO^-_{PW}). Regarding the decay stage of NAO^-_{NW}, baroclinic energy conversion becomes the dominant factor that maintains the excessive K^1 during that time (cf. the significant difference of B^1 between the two interannual regimes in Fig. 10f). It is interesting to note that the inverse cascade process during the decay stage does not show a clear difference between the NAO^-_{PW} and the NAO^-_{NW}, even though there exists a significant difference between the K^2 reservoir for the two regimes in this period (Fig. 8b). The magnitudes of the nonlocal and dissipation processes exhibit complex variations during the life cycle of the NAO^-_{PW} and NAO^-_{NW}, although differences between the two regimes are not statistically significant at the 90% level at most lags due to their strong variance. Generally, both two processes act to balance the excessive K^1 during the life cycles of the two regimes. In other words, they are not a cause of the distinct intraseasonal variability as observed in the two interannual NAO regimes.

c. *Role of the jet stream*

The above energetics analysis suggests a linkage between the North Atlantic jet stream and the anomalous NAO flow.

On one hand, the jet stream directly feeds the NAO flow through barotropic instability. On the other hand, the strength of the jet stream modulates the high-frequency synoptic transients by baroclinic instability, which further exerts its feedback on the slow-varying NAO flow via inverse cascades. In addition, the jet stream may also influence the energy dispersion by changing the meridional PV gradient as suggested by Luo et al. (2018). In the following, we present the regime-dependent feature of the above-mentioned processes from the perspective of the role of jet stream.

For the NAO^+ events, the jet stream is more intensified during the life cycle of NAO^+_{PW} than that of NAO^+_{NW}. From Fig. 17 (black contours), it can be seen that the core of the jet stream is more zonally spread out across the NAO region during the segment from lag −2 to +4 days of NAO^+_{PW} than that of NAO^+_{NW}. This creates larger meridional temperature gradient and thus larger baroclinic energy conversion to synoptic transients during the life cycle of NAO^+_{PW} (Fig. 18). However, as mentioned previously, larger baroclinic generation rates do not necessarily lead to stronger inverse cascades. The strength of inverse cascades is not only dependent on the strength of baroclinic instability, but is also dependent on the dispersion process modulated by the background jet stream. To see this, we further analyze the magnitude of PV_y, which has been used to quantify the strength of energy dispersion in the North Atlantic jet region (Luo et al. 2018). According to Luo et al. (2018), enhanced (reduced) PV_y is indicative of enhanced (reduced) energy dispersion. Indeed, as shown in Fig. 17 (color shading), the magnitude of PV_y is significantly larger for NAO^+_{PW} than NAO^+_{NW} in the NAO region. This confirms that the stronger jet stream during the life cycle of NAO^+_{PW} causes more energy dispersion, and thus leads to the suppression of inverse cascades.

Another possible factor that may influence the strength of inverse cascades is the lateral shear created by the jet stream. Robert et al. (2017) identified a negative eddy feedback in their three-level quasigeostrophic model: the enhanced meridional wind shear associated with the acceleration of the jet tends to increase the barotropic inverse cascades and hence weaken the synoptic eddies. This mechanism does not seem to apply to the asymmetry of eddy feedback between the two interannual regimes. In our case, the wind shear is larger for NAO^+_{PW} than NAO^+_{NW}, whereas the inverse cascade is larger for NAO^+_{NW} than NAO^+_{PW}.

Regarding the NAO^- events, the early stage of NAO^-_{PW} is characterized by a more enhanced and northward-shifted jet compared to that of NAO^-_{NW} (black contours in Fig. 19). Similar to the scenario mentioned above, the large energy dispersion (large PV_y) is likely responsible for the weak inverse cascade in this segment of NAO^-_{PW}, albeit with enhanced level of baroclinic instability (Figs. 8f and 20). In contrast, the relationship between the jet stream and the inverse cascades in the peak and decay stages seems more straightforward. That is, the stronger jet creates more synoptic transients via baroclinic instability which in turn leads to more efficient inverse cascades. The PV_y is relatively in the NAO region during these stages in the NAO region, suggesting that the influence of energy dispersion on the inverse cascade is limited (color shading in Fig. 19).

The above results provide evidence that the relation between the North Atlantic jet stream, synoptic transients, and inverse cascading process is more complex than that suggested in previous studies (e.g., Branstator 1992; Lorenz and Hartmann 2003; Barnes and Hartmann 2010), especially when considering the interannual regimes of the NAO events. More work is needed to reveal the underlying dynamics, which will be the task of future investigations.

5. Conclusions and discussion

The interannual variability of the NAO events is investigated using the 142-yr (1871–2012) 20CR data, and a novel, time-dependent, and spatially localized energetics analysis is employed to examine the dynamics of the asymmetry between the interannual NAO regimes. Three orthogonal scale windows, namely, a seasonal mean flow window, an intraseasonal-scale window, and a synoptic-scale window, are introduced with the aid of the MWT (Liang and Anderson 2007). The nonlinear energy transfers between these scale windows are diagnosed using the theory of canonical transfer in light of energy conservation across scales (Liang 2016). Based on a wintertime mean NAO index and a daily NAO index, four subgroups of typical events are identified, i.e., NAO^+ events in positive (negative) NAO winter regime and NAO^- events in positive (negative) NAO winter regime, which are denoted as NAO^+_{PW}, NAO^+_{NW}, NAO^-_{PW}, and NAO^-_{NW}, respectively. Analyses of the statistics, spatiotemporal characteristics, and energetics of these subgroup events lead to the following conclusions.

The interannual NAO regime reflects the ensemble mean of NAO events occurring on the intraseasonal time scale. The positive interannual NAO regime is dominated by higher (lower) occurrence frequency of NAO^+_{PW} (NAO^-_{PW}) events, with more (less) persistent lifespan and enhanced (reduced) intensity, whereas the negative interannual NAO regime is dominant by higher (lower) frequency of occurrence of NAO^-_{NW} (NAO^+_{NW}) events, with more (less) persistent lifespan and enhanced (reduced) intensity.

In general, NAO^- (NAO^+) is associated with enhanced (reduced) intraseasonal variability and thus larger (smaller) K^1 in the North Atlantic sector. However, the energetics features are distinctly different between interannual regimes, indicating different dynamical sources of these regimes. It is found that K^1 is significantly enhanced for the NAO^+_{NW} compared to that for the NAO^+_{PW}, mainly due to episodical bursts of inverse cascade process from synoptic transients and reduced energy dispersion during the life cycle of the NAO^+_{NW}. Regarding the negative-phase events, significantly larger amplitude of K^1 is observed in the early and decay stages of NAO^-_{NW} than NAO^-_{PW}, whereas the reverse occurs in the peak stage. Both the inverse cascades and baroclinic energy conversion play important roles in the formation of excessive K^1 in the early stage of NAO^-_{NW}, whereas only the latter contributes to the larger K^1 during the decay stage of NAO^-_{NW} compared to that of the NAO^-_{PW}. The barotropic transfer

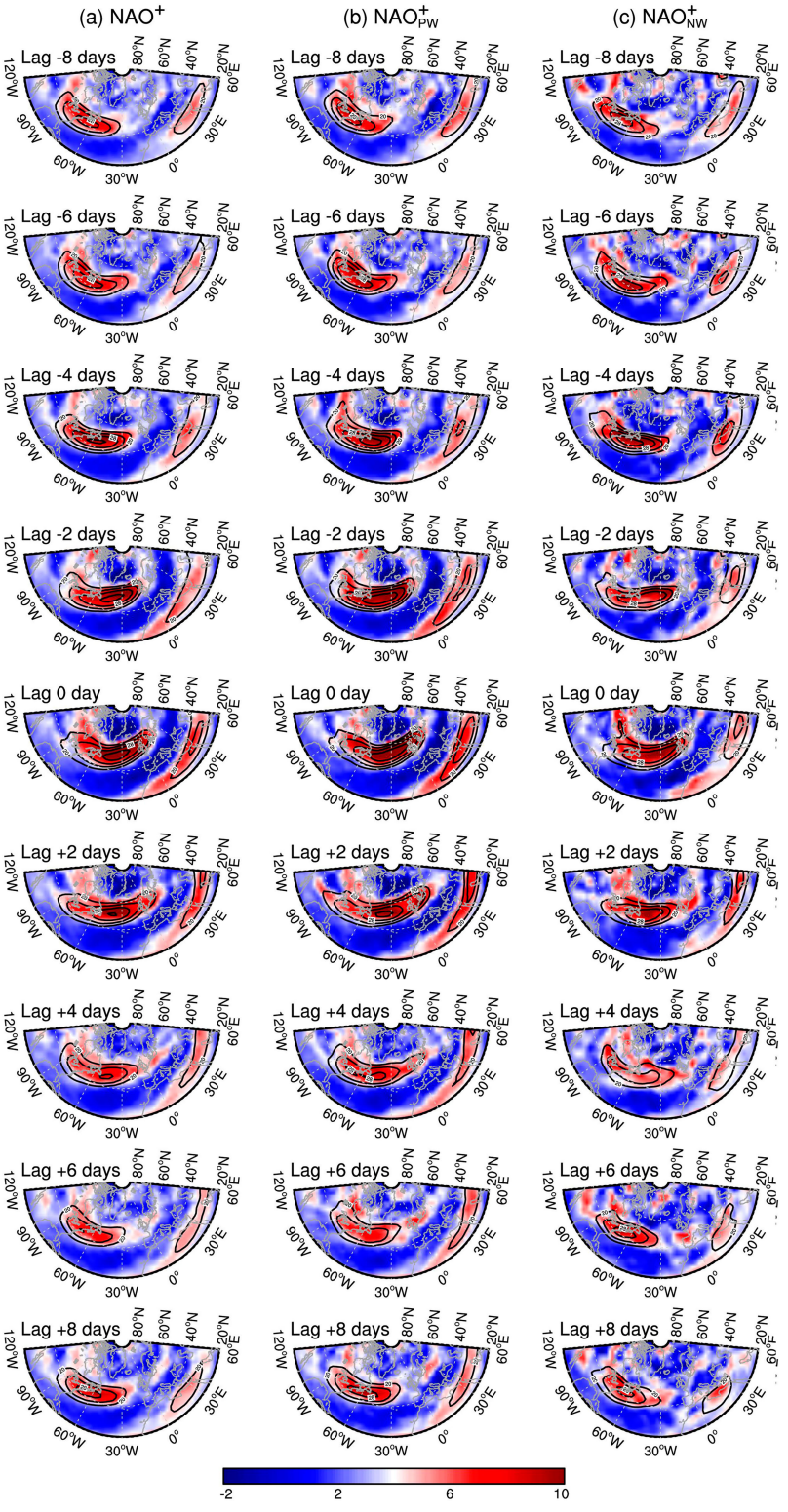

FIG. 17. Time-evolution spatial patterns of PV_y (unit: 10^{-13} K m^2 kg^{-1} s^{-1}) and zonal velocity (black contours; CI: 4 m s^{-1} starting from 20 m s^{-1}) at 300 hPa for (a) NAO^+, (b) NAO^+_{PW}, and (c) NAO^+_{NW}.

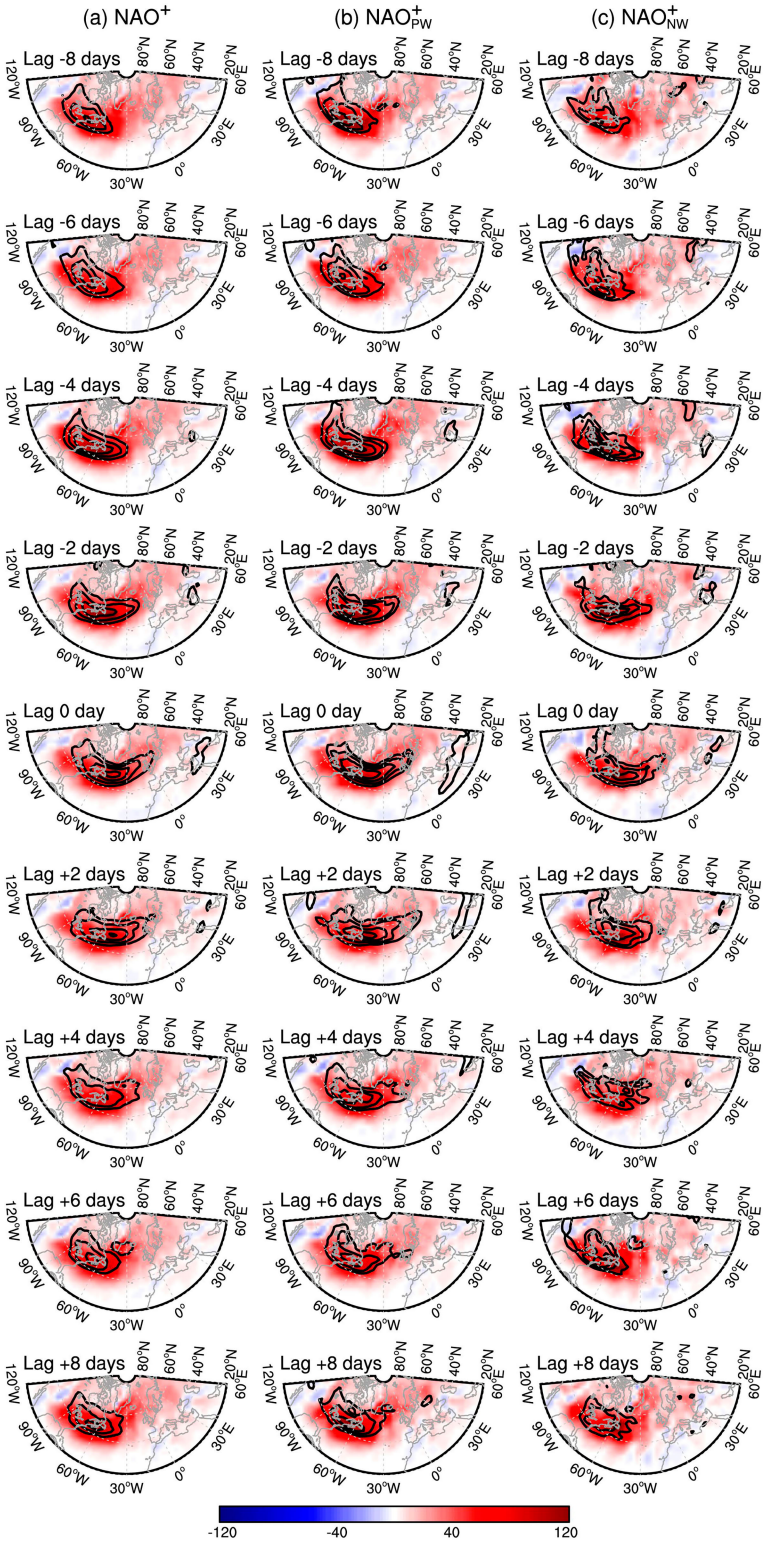

FIG. 18. Time-evolution spatial patterns of the vertically averaged (1000–100 hPa) B^2 (color shading; unit: 10^{-5} m^2 s^{-3}) and the meridional temperature gradient (black contours; CI: 10^{-6} K m^{-1} starting from 6×10^{-6} K m^{-1}) at 300 hPa for (a) NAO$^+$, (b) NAO$^+_{\mathrm{PW}}$, and (c) NAO$^+_{\mathrm{NW}}$.

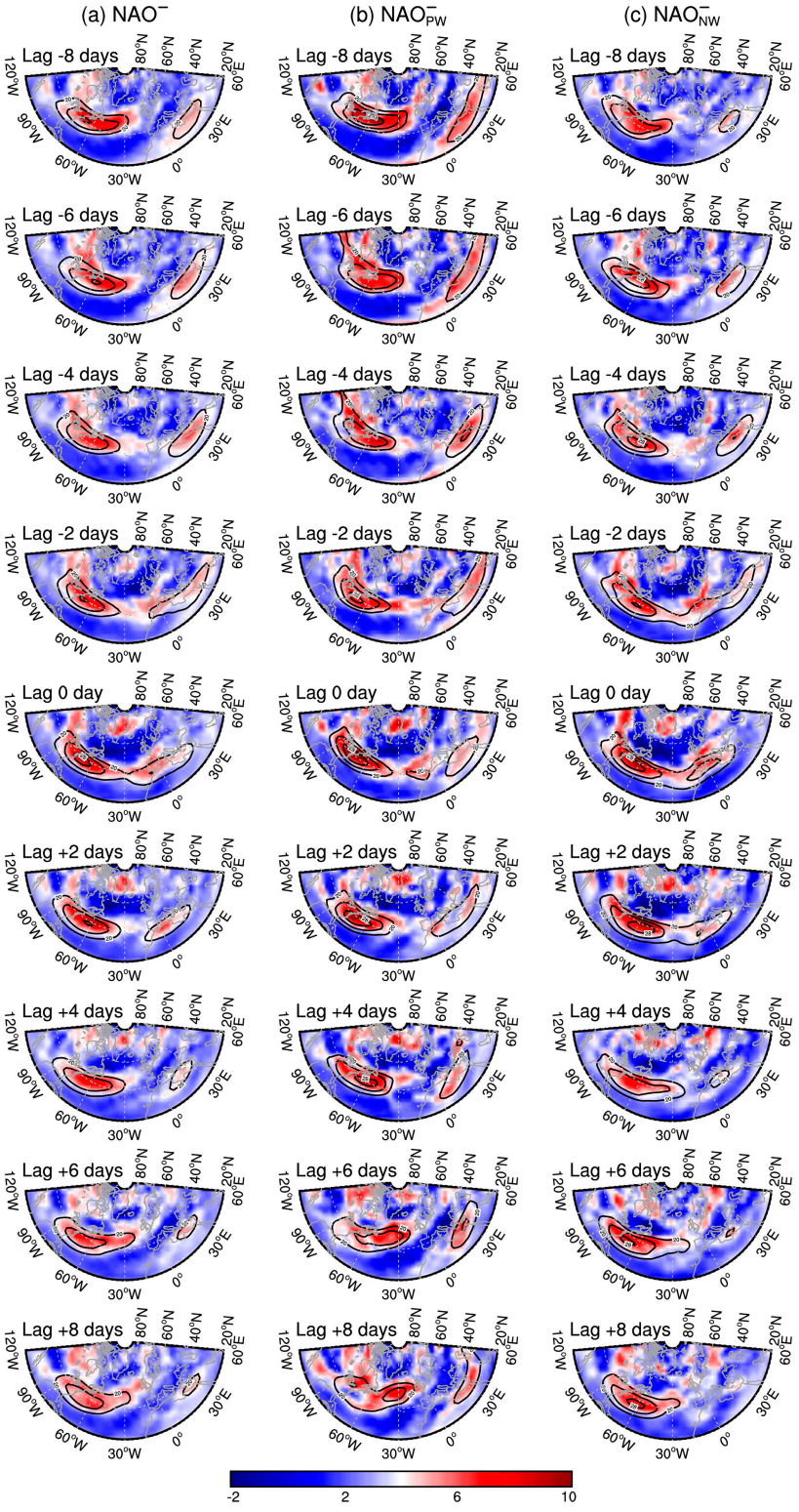

FIG. 19. As in Fig. 17, but for (a) NAO^-, (b) NAO^-_{PW}, and (c) NAO^-_{NW}.

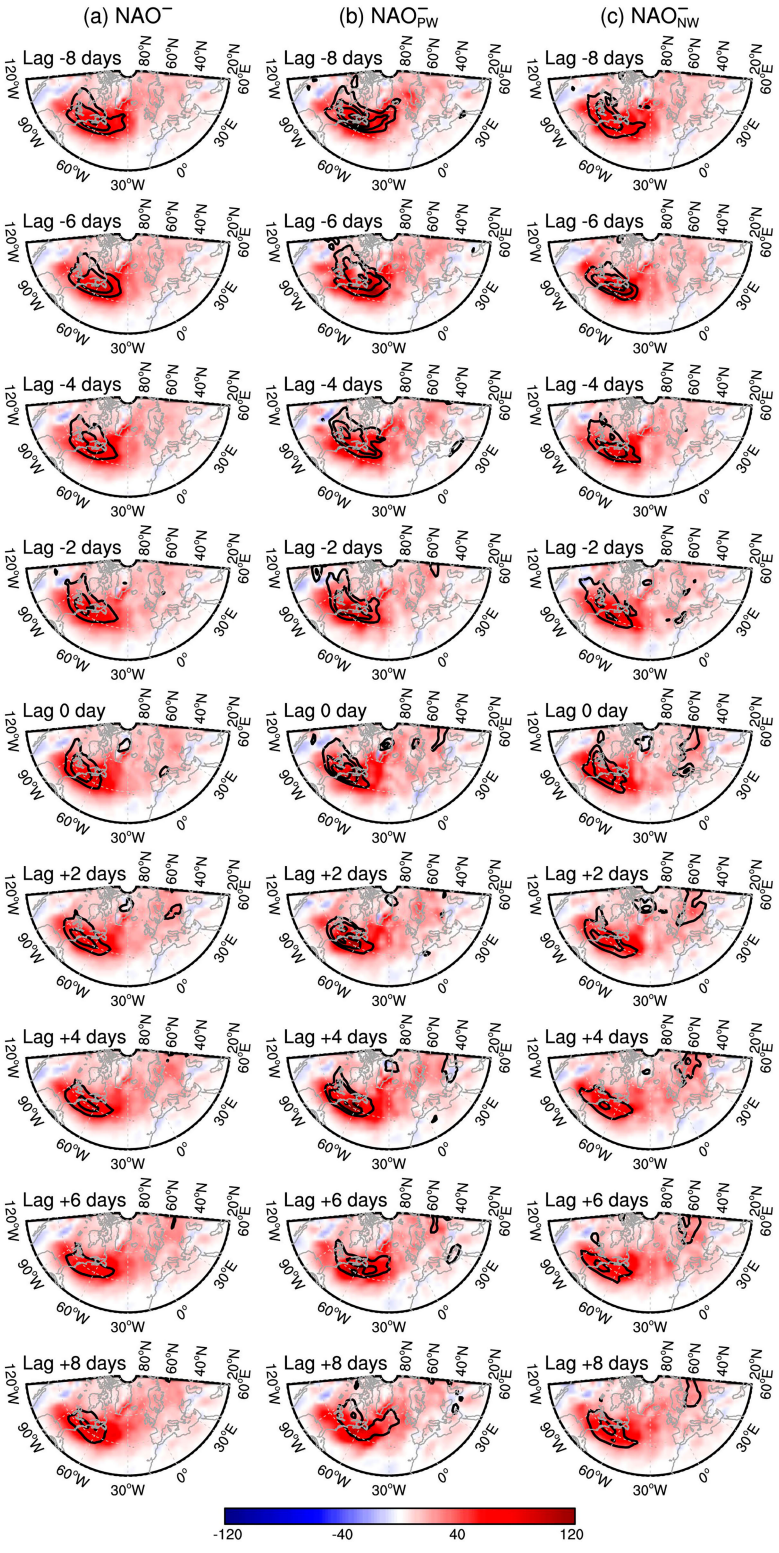

FIG. 20. As in Fig. 18, but for (a) NAO^-, (b) NAO^-_{PW}, and (c) NAO^-_{NW}.

from the mean flow, inverse cascades, and baroclinic energy conversion are all responsible for the strengthened K^1 in the peak stage of NAO^-_{PW}.

Our results suggest that the essential dynamical processes that control the growth and decay of the intraseasonal NAO events, including the barotropic transfers from the mean flow and synoptic transients, the baroclinic energy conversion, and energy dispersion, are not only phase dependent, but also regime dependent on the interannual and longer time scales. An implication of this analysis is that events that fall on different interannual regimes should be considered separately, otherwise it may be difficult to identify the relevant mechanisms due to the large offset of certain processes between different regimes. An example of this is the inverse cascade process which even exhibits out-of-phase variations during the life cycles of events with the same phase but different interannual regimes (see Figs. 10c and 7d).

Another interesting result revealed by our analysis is that the barotropic energy transfer from the mean flow to the intraseasonal-scale flow, whose amplitude is generally correlated with the growth and decay of K^1 for both positive- and negative-phase events, is not responsible for the K^1 asymmetry between the two interannual regimes, except for the peak stage of NAO^-_{PW} and NAO^-_{NW}. The enhanced barotropic transfer during the positive NAO winters (for both phases) reflects the interannual modulation of the jet stream intensity, i.e., on the interannual time scale, the strengthening of the jet stream leads to enhanced barotropic instability, and thus enhanced KE transfer from the mean flow to the intraseasonal-scale flow. However, we have already seen that overall, this is not responsible for the distinction between regimes.

Our results also highlight the important role played by the baroclinic energy conversion in the formation and maintenance of the NAO events, which is usually not considered in classical models used to investigate the NAO (e.g., Simmons et al. 1983; Jin et al. 2006; Luo et al. 2015). In particular, the baroclinic process is found to dominate the energy sources of the intraseasonal variability in the early and decay stages of the NAO^-_{NW} events.

A limitation of this study is that the sample sizes of some composite groups (e.g., NAO^+_{NW} and NAO^-_{PW}) may not be large enough in the application of statistical significance tests. Due to the rather chaotic behavior of the synoptic transients during the life cycle of the NAO event, a faithful statistics of the diagnostic metrics associated with the synoptic transients (e.g., K^2 and $\Gamma_K^{2\to1}$; see their temporal evolutions for individual events in Figs. S2 and S3 in the supplementary material) for the PW and NW interannual regimes may require much longer dataset than the present 142-yr-long 20CR data used in this study. Future study with longer dataset and idealized experiments is needed to check and justify the statistical significance of the impact of synoptic-related processes to different phases and regimes of the NAO.

In this study, the role of the ocean–atmosphere coupling and external forcings such as solar radiation and volcanic eruption in the asymmetry between the interannual NAO regimes are not considered. Previous studies have shown that the NAO can drive large-scale SST changes in the North Atlantic, which in turn modify the NAO variability through thermal feedback processes (e.g., Rodwell et al. 1999; Robertson et al. 2000; Peng et al. 2003; Czaja et al. 2003). Besides, the interannual to decadal variations of the NAO have been found to be modulated by the phase of the solar cycle (e.g., Kodera 2002; Ineson et al. 2011; Gray et al. 2013) and the volcanic activity (e.g., Stenchikov et al. 2002; Christiansen 2008; Ortega et al. 2015; Qu et al. 2021). These external processes are not necessarily exclusive with the intrinsic atmospheric processes as focused on in the present study, because they are likely to influence the asymmetry by modulating the strength and frequency of the intrinsic dynamical processes such as the interaction between the background jet and the NAO flow and the inverse cascades. Further studies are needed to understand the influences of these forcings on the long-term change of the NAO.

Acknowledgments. The constructive suggestions of two anonymous reviewers are appreciated. YY thanks Jiwang Ma and Yineng Rong for valuable discussions. Fruitful discussions with Dr. Dehai Luo at the Seventh Nonlinear Atmosphere–Ocean Sciences Workshop are also appreciated. This research is supported by National Science Foundation of China (NSFC) (Grants 41975064, 42276017, and 42230105), by Southern Marine Science and Engineering Guangdong Laboratory (Zhuhai) (313022005, SML2023SP203), by Fudan University (IDH2318009Y), by Shanghai B & R Joint Laboratory Project (Grant 22230750300), and by Shanghai International Science and Technology Partnership Project (Grant 21230780200).

Data availability statement. The 20CR data are available at https://psl.noaa.gov/data/gridded/data.20thC_ReanV2.html. The MWT and energetics analysis package are available at http://www.ncoads.org/.

REFERENCES

Ayarzagüena, B., S. Ineson, N. J. Dunstone, M. P. Baldwin, and A. A. Scaife, 2018: Intraseasonal effects of El Niño–Southern Oscillation on North Atlantic climate. *J. Climate*, **31**, 8861–8873, https://doi.org/10.1175/JCLI-D-18-0097.1.

Barnes, E. A., and D. L. Hartmann, 2010: Dynamical feedbacks and the persistence of the NAO. *J. Atmos. Sci.*, **67**, 851–865, https://doi.org/10.1175/2009JAS3193.1.

Benedict, J. J., S. Lee, and S. B. Feldstein, 2004: Synoptic view of the North Atlantic Oscillation. *J. Atmos. Sci.*, **61**, 121–144, https://doi.org/10.1175/1520-0469(2004)061<0121:SVOTNA>2.0.CO;2.

Branstator, G., 1992: The maintenance of low-frequency atmospheric anomalies. *J. Atmos. Sci.*, **49**, 1924–1946, https://doi.org/10.1175/1520-0469(1992)049<1924:TMOLFA>2.0.CO;2.

Bretherton, C. S., and D. S. Battisti, 2000: An interpretation of the results from atmospheric general circulation models forced by the time history of the observed sea surface temperature distribution. *Geophys. Res. Lett.*, **27**, 767–770, https://doi.org/10.1029/1999GL010910.

Brönnimann, S., 2007: Impact of El Niño–Southern Oscillation on European climate. *Rev. Geophys.*, **45**, RG3003, https://doi.org/10.1029/2006RG000199.

Cai, M., and M. Mak, 1990: Symbiotic relation between planetary and synoptic-scale waves. *J. Atmos. Sci.*, **47**, 2953–2968, https://doi.org/10.1175/1520-0469(1990)047<2953:SRBPAS>2.0.CO;2.

Cassou, C., L. Terray, J. W. Hurrell, and C. Deser, 2004: North Atlantic winter climate regimes: Spatial asymmetry, stationarity with time, and oceanic forcing. *J. Climate*, **17**, 1055–1068, https://doi.org/10.1175/1520-0442(2004)017<1055:NAWCRS>2.0.CO;2.

Castanheira, J. M., and C. A. F. Marques, 2019: The energy cascade associated with daily variability of the North Atlantic Oscillation. *Quart. J. Roy. Meteor. Soc.*, **145**, 197–210, https://doi.org/10.1002/qj.3422.

Christiansen, B., 2008: Volcanic eruptions, large-scale modes in the Northern Hemisphere, and the El Niño–Southern Oscillation. *J. Climate*, **21**, 910–922, https://doi.org/10.1175/2007JCLI1657.1.

Ciasto, L. M., and D. W. J. Thompson, 2004: North Atlantic atmosphere–ocean interaction on intraseasonal time scales. *J. Climate*, **17**, 1617–1621, https://doi.org/10.1175/1520-0442(2004)017<1617:NAAIOI>2.0.CO;2.

Cohen, J., A. Frei, and R. D. Rosen, 2005: The role of boundary conditions in AMIP-2 simulations of the NAO. *J. Climate*, **18**, 973–981, https://doi.org/10.1175/JCLI-3305.1.

Compo, G. P., and Coauthors, 2011: The Twentieth Century Reanalysis project. *Quart. J. Roy. Meteor. Soc.*, **137**, 1–28, https://doi.org/10.1002/qj.776.

Czaja, A., A. W. Robertson, and T. Huck, 2003: The role of Atlantic ocean-atmosphere coupling in affecting North Atlantic Oscillation variability. *The North Atlantic Oscillation: Climatic Significance and Environmental Impact*, Amer. Geophys. Union, 147–172.

DeWeaver, E., and S. Nigam, 2000: Zonal-eddy dynamics of the North Atlantic Oscillation. *J. Climate*, **13**, 3893–3914, https://doi.org/10.1175/1520-0442(2000)013<3893:ZEDOTN>2.0.CO;2.

Feldstein, S. B., 2000: The timescale, power spectra, and climate noise properties of teleconnection patterns. *J. Climate*, **13**, 4430–4440, https://doi.org/10.1175/1520-0442(2000)013<4430:TTPSAC>2.0.CO;2.

——, 2003: The dynamics of NAO teleconnection pattern growth and decay. *Quart. J. Roy. Meteor. Soc.*, **129**, 901–924, https://doi.org/10.1256/qj.02.76.

Franzke, C., 2009: Multi-scale analysis of teleconnection indices: Climate noise and nonlinear trend analysis. *Nonlinear Processes Geophys.*, **16**, 65–76, https://doi.org/10.5194/npg-16-65-2009.

Frederiksen, J. S., 1983: A unified three-dimensional instability theory of the onset of blocking and cyclogenesis. II. Teleconnection patterns. *J. Atmos. Sci.*, **40**, 2593–2609, https://doi.org/10.1175/1520-0469(1983)040<2593:AUTDIT>2.0.CO;2.

Gray, L. J., and Coauthors, 2013: A lagged response to the 11 year solar cycle in observed winter Atlantic/European weather patterns. *J. Geophys. Res. Atmos.*, **118**, 13 405–13 420, https://doi.org/10.1002/2013JD020062.

Higgins, R. W., and S. D. Schubert, 1994: Simulated life cycles of persistent anticyclonic anomalies over the North Pacific: Role of synoptic-scale eddies. *J. Atmos. Sci.*, **51**, 3238–3260, https://doi.org/10.1175/1520-0469(1994)051<3238:SLCOPA>2.0.CO;2.

Holopainen, E. O., 1978: A diagnostic study of the kinetic energy balance of the long-term mean flow and the associated transient fluctuations in the atmosphere. *Geophysica*, **15**, 125–145, https://www.geophysica.fi/pdf/geophysica_1978_15_1_125_holopainen.pdf.

Hoskins, B. J., I. N. James, and G. H. White, 1983: The shape, propagation and mean-flow interaction of large-scale weather systems. *J. Atmos. Sci.*, **40**, 1595–1612, https://doi.org/10.1175/1520-0469(1983)040<1595:TSPAMF>2.0.CO;2.

Hurrell, J. W., 1995: Decadal trends in the North Atlantic Oscillation: Regional temperatures and precipitation. *Science*, **269**, 676–679, https://doi.org/10.1126/science.269.5224.676.

——, Y. Kushnir, G. Ottersen, and M. Visbeck, 2003: An overview of the North Atlantic Oscillation. *The North Atlantic Oscillation: Climatic Significance and Environmental Impact*, Amer. Geophys. Union, 1–35.

Ineson, S., A. A. Scaife, J. R. Knight, J. C. Manners, N. J. Dunstone, L. J. Gray, and J. D. Haigh, 2011: Solar forcing of winter climate variability in the Northern Hemisphere. *Nat. Geosci.*, **4**, 753–757, https://doi.org/10.1038/ngeo1282.

Jia, X. J., J. Derome, and H. Lin, 2007: Comparison of the life cycles of the NAO using different definitions. *J. Climate*, **20**, 5992–6011, https://doi.org/10.1175/2007JCLI1408.1.

Jiang, T., Y. Deng, and W. Li, 2013: Local kinetic energy budget of high-frequency and intermediate-frequency eddies: Winter climatology and interannual variability. *Climate Dyn.*, **41**, 961–976, https://doi.org/10.1007/s00382-013-1684-1.

Jin, F.-F., L.-L. Pan, and M. Watanabe, 2006: Dynamics of synoptic eddy and low-frequency flow interaction. Part II: A theory for low-frequency modes. *J. Atmos. Sci.*, **63**, 1695–1708, https://doi.org/10.1175/JAS3716.1.

Johnson, N. C., S. B. Feldstein, and B. Tremblay, 2008: The continuum of Northern Hemisphere teleconnection patterns and a description of the NAO shift with the use of self-organizing maps. *J. Climate*, **21**, 6354–6371, https://doi.org/10.1175/2008JCLI2380.1.

Josey, S. A., E. C. Kent, and B. Sinha, 2001: Can a state of the art atmospheric general circulation model reproduce recent NAO related variability at the air-sea interface? *Geophys. Res. Lett.*, **28**, 4543–4546, https://doi.org/10.1029/2001GL013200.

Kodera, K., 2002: Solar cycle modulation of the North Atlantic Oscillation: Implication in the spatial structure of the NAO. *Geophys. Res. Lett.*, **29**, 1218, https://doi.org/10.1029/2001GL014557.

Kunz, T., K. Fraedrich, and F. Lunkeit, 2009: Impact of synoptic-scale wave breaking on the NAO and its connection with the stratosphere in ERA-40. *J. Climate*, **22**, 5464–5480, https://doi.org/10.1175/2009JCLI2750.1.

Lau, N.-C., 1988: Variability of the observed midlatitude storm tracks in relation to low-frequency changes in the circulation pattern. *J. Atmos. Sci.*, **45**, 2718–2743, https://doi.org/10.1175/1520-0469(1988)045<2718:VOTOMS>2.0.CO;2.

Liang, X. S., 2016: Canonical transfer and multiscale energetics for primitive and quasigeostrophic atmospheres. *J. Atmos. Sci.*, **73**, 4439–4468, https://doi.org/10.1175/JAS-D-16-0131.1.

——, and A. R. Robinson, 2005: Localized multiscale energy and vorticity analysis: I. Fundamentals. *Dyn. Atmos. Oceans*, **38**, 195–230, https://doi.org/10.1016/j.dynatmoce.2004.12.004.

——, and D. G. M. Anderson, 2007: Multiscale window transform. *Multiscale Model. Simul.*, **6**, 437–467, https://doi.org/10.1137/06066895X.

——, and A. R. Robinson, 2007: Localized multi-scale energy and vorticity analysis: II. Finite-amplitude instability theory and validation. *Dyn. Atmos. Oceans*, **44**, 51–76, https://doi.org/10.1016/j.dynatmoce.2007.04.001.

Lorenz, D. J., and D. L. Hartmann, 2003: Eddy–zonal flow feedback in the Northern Hemisphere winter. *J. Climate*, **16**, 1212–1227, https://doi.org/10.1175/1520-0442(2003)16<1212:EFFITN>2.0.CO;2.

Lorenz, E. N., 1955: Available potential energy and the maintenance of the general circulation. *Tellus*, **7**, 157–167, https://doi.org/10.3402/tellusa.v7i2.8796.

Luo, D., Y. Diao, and S. B. Feldstein, 2011: The variability of the Atlantic storm track and the North Atlantic Oscillation: A link between intraseasonal and interannual variability. *J. Atmos. Sci.*, **68**, 577–601, https://doi.org/10.1175/2010JAS3579.1.

——, J. Cha, and S. B. Feldstein, 2012: Weather regime transitions and the interannual variability of the North Atlantic Oscillation. Part I: A likely connection. *J. Atmos. Sci.*, **69**, 2329–2346, https://doi.org/10.1175/JAS-D-11-0289.1.

——, L. Zhong, and C. L. E. Franzke, 2015: Inverse energy cascades in an eddy-induced NAO-type flow: Scale interaction mechanism. *J. Atmos. Sci.*, **72**, 3417–3448, https://doi.org/10.1175/JAS-D-15-0062.1.

——, X. Chen, and S. B. Feldstein, 2018: Linear and nonlinear dynamics of North Atlantic Oscillations: A new thinking of symmetry breaking. *J. Atmos. Sci.*, **75**, 1955–1977, https://doi.org/10.1175/JAS-D-17-0274.1.

Ma, J., and X. S. Liang, 2023: Distinctly different dynamical processes in maintaining the intraseasonal NAO+ and NAO−. *Geophys. Res. Lett.*, **50**, e2023GL103351, https://doi.org/10.1029/2023GL103351.

Martineau, P., H. Nakamura, Y. Kosaka, and A. Yamamoto, 2020: Importance of a vertically tilting structure for energizing the North Atlantic Oscillation. *Sci. Rep.*, **10**, 12671, https://doi.org/10.1038/s41598-020-69551-5.

Nakamura, H., and J. M. Wallace, 1990: Observed changes in baroclinic wave activity during the life cycles of low-frequency circulation anomalies. *J. Atmos. Sci.*, **47**, 1100–1116, https://doi.org/10.1175/1520-0469(1990)047<1100:OCIBWA>2.0.CO;2.

Nie, Y., H.-L. Ren, and Y. Zhang, 2019: The role of extratropical air–sea interaction in the autumn subseasonal variability of the North Atlantic Oscillation. *J. Climate*, **32**, 7697–7712, https://doi.org/10.1175/JCLI-D-19-0060.1.

Orlanski, I., and J. Katzfey, 1991: The life cycle of a cyclone wave in the Southern Hemisphere. Part I: Eddy energy budget. *J. Atmos. Sci.*, **48**, 1972–1998, https://doi.org/10.1175/1520-0469(1991)048<1972:TLCOAC>2.0.CO;2.

Ortega, P., F. Lehner, D. Swingedouw, V. Masson-Delmotte, C. C. Raible, M. Casado, and P. Yiou, 2015: A model-tested North Atlantic Oscillation reconstruction for the past millennium. *Nature*, **523**, 71–74, https://doi.org/10.1038/nature14518.

Peng, S., W. A. Robinson, and S. Li, 2003: Mechanisms for the NAO responses to the North Atlantic SST tripole. *J. Climate*, **16**, 1987–2004, https://doi.org/10.1175/1520-0442(2003)016<1987:MFTNRT>2.0.CO;2.

Plumb, R. A., 1983: A new look at the energy cycle. *J. Atmos. Sci.*, **40**, 1669–1688, https://doi.org/10.1175/1520-0469(1983)040<1669:ANLATE>2.0.CO;2.

Qu, W., F. Huang, J. Zhao, L. Du, and Y. Cao, 2021: Volcanic activity sparks the Arctic Oscillation. *Sci. Rep.*, **11**, 15839, https://doi.org/10.1038/s41598-021-94935-6.

Ren, H.-L., F.-F. Jin, and L. Gao, 2012: Anatomy of synoptic eddy–NAO interaction through eddy structure decomposition. *J. Atmos. Sci.*, **69**, 2171–2191, https://doi.org/10.1175/JAS-D-11-069.1.

Rennert, K. J., and J. M. Wallace, 2009: Cross-frequency coupling, skewness, and blocking in the Northern Hemisphere winter circulation. *J. Climate*, **22**, 5650–5666, https://doi.org/10.1175/2009JCLI2669.1.

Rivière, G., and I. Orlanski, 2007: Characteristics of the Atlantic storm-track eddy activity and its relation with the North Atlantic Oscillation. *J. Atmos. Sci.*, **64**, 241–266, https://doi.org/10.1175/JAS3850.1.

Robert, L., G. Rivière, and F. Codron, 2017: Positive and negative eddy feedbacks acting on midlatitude jet variability in a three-level quasigeostrophic model. *J. Atmos. Sci.*, **74**, 1635–1649, https://doi.org/10.1175/JAS-D-16-0217.1.

Robertson, A. W., C. R. Mechoso, and Y.-J. Kim, 2000: The influence of Atlantic sea surface temperature anomalies on the North Atlantic Oscillation. *J. Climate*, **13**, 122–138, https://doi.org/10.1175/1520-0442(2000)013<0122:TIOASS>2.0.CO;2.

Robinson, W. A., 2000: A baroclinic mechanism for the eddy feedback on the zonal index. *J. Atmos. Sci.*, **57**, 415–422, https://doi.org/10.1175/1520-0469(2000)057<0415:ABMFTE>2.0.CO;2.

Rodwell, M. J., D. P. Rowell, and C. K. Folland, 1999: Oceanic forcing of the wintertime North Atlantic Oscillation and European climate. *Nature*, **398**, 320–323, https://doi.org/10.1038/18648.

Saltsman, B., 1957: Equations governing the energetics of the larger scales of atmospheric turbulence in the domain of wave number. *J. Meteor.*, **14**, 513–523, https://doi.org/10.1175/1520-0469(1957)014<0513:EGTEOT>2.0.CO;2.

Schmith, T., S. M. Olsen, S. Yang, and J. H. Christensen, 2022: Asymmetries in circulation anomalies related to the phases of the North Atlantic Oscillation on synoptic time scales. *Geophys. Res. Lett.*, **49**, e2022GL098149, https://doi.org/10.1029/2022GL098149.

Sheng, J., and J. Derome, 1991: An observational study of the energy transfer between the seasonal mean flow and transient eddies. *Tellus*, **43A**, 128–144, https://doi.org/10.3402/tellusa.v43i2.11921.

Simmons, A. J., J. M. Wallace, and G. W. Branstator, 1983: Barotropic wave propagation and instability, and atmospheric teleconnection patterns. *J. Atmos. Sci.*, **40**, 1363–1392, https://doi.org/10.1175/1520-0469(1983)040<1363:BWPAIA>2.0.CO;2.

Song, J., 2016: Understanding anomalous eddy vorticity forcing in North Atlantic Oscillation events. *J. Atmos. Sci.*, **73**, 2985–3007, https://doi.org/10.1175/JAS-D-15-0253.1.

Stenchikov, G., A. Robock, V. Ramaswamy, M. D. Schwarzkopf, K. Hamilton, and S. Ramachandran, 2002: Arctic Oscillation response to the 1991 Mount Pinatubo eruption: Effects of volcanic aerosols and ozone depletion. *J. Geophys. Res.*, **107**, 4803, https://doi.org/10.1029/2002JD002090.

Thompson, D. W. J., S. Lee, and M. P. Baldwin, 2003: Atmospheric processes governing the Northern Hemisphere Annular Mode/North Atlantic Oscillation. *The North Atlantic Oscillation: Climatic Significance and Environmental Impact*, Amer. Geophys. Union, 81–112.

Vallis, G. K., E. P. Gerber, P. J. Kushner, and B. A. Cash, 2004: A mechanism and simple dynamical model of the North Atlantic Oscillation and annular modes. *J. Atmos. Sci.*, **61**, 264–280, https://doi.org/10.1175/1520-0469(2004)061<0264:AMASDM>2.0.CO;2.

Wallace, J. M., and D. S. Gutzler, 1981: Teleconnections in the geopotential height field during the Northern Hemisphere winter. *Mon. Wea. Rev.*, **109**, 784–812, https://doi.org/10.1175/1520-0493(1981)109<0784:TITGHF>2.0.CO;2.

Watanabe, M., M. Kimoto, T. Nitta, and M. Kachi, 1999: A comparison of decadal climate oscillations in the North Atlantic detected in observations and a coupled GCM. *J. Climate*, **12**, 2920–2940, https://doi.org/10.1175/1520-0442(1999)012<2920:ACODCO>2.0.CO;2.

Whitaker, J. S., and T. M. Hamill, 2002: Ensemble data assimilation without perturbed observations. *Mon. Wea. Rev.*, **130**, 1913–1924, https://doi.org/10.1175/1520-0493(2002)130<1913:EDAWPO>2.0.CO;2.

Woollings, T., B. Hoskins, M. Blackburn, and P. Berrisford, 2008: A new Rossby wave–breaking interpretation of the North Atlantic Oscillation. *J. Atmos. Sci.*, **65**, 609–626, https://doi.org/10.1175/2007JAS2347.1.

——, A. Hannachi, and B. Hoskins, 2010: Variability of the North Atlantic eddy-driven jet stream. *Quart. J. Roy. Meteor. Soc.*, **136**, 856–868, https://doi.org/10.1002/qj.625.

——, C. Franzke, D. L. R. Hodson, B. Dong, E. A. Barnes, C. C. Raible, and J. G. Pinto, 2015: Contrasting interannual and multidecadal NAO variability. *Climate Dyn.*, **45**, 539–556, https://doi.org/10.1007/s00382-014-2237-y.

Yang, Y., and X. S. Liang, 2019: New perspectives on the generation and maintenance of the Kuroshio large meander. *J. Phys. Oceanogr.*, **49**, 2095–2113, https://doi.org/10.1175/JPO-D-18-0276.1.

Zhao, S., H.-L. Ren, F. Zhou, A. A. Scaife, and Y. Nie, 2023: Phase asymmetry in synoptic eddy feedbacks on the negatively-skewed winter NAO. *Atmos. Res.*, **288**, 106725, https://doi.org/10.1016/j.atmosres.2023.106725.